

1 **A muographic study of a scoria cone from 11**  
2 **directions using nuclear emulsion cloud chambers**

3

4 Seigo Miyamoto<sup>1</sup>, Shogo Nagahara<sup>1,2</sup>, Kunihiro Morishima<sup>3</sup>, Toshiyuki Nakano<sup>3</sup>,  
5 Masato Koyama<sup>4</sup>, Yusuke Suzuki<sup>5</sup>

6

7 <sup>1</sup>Earthquake Research Institute, The University of Tokyo, 1-1-1 Yayoi, Bunkyo-ku,  
8 Tokyo, 113-0032, Japan.

9 <sup>2</sup>Graduate School of Human Development and Environment, Kobe University, 3-11  
10 Tsurukabuto, Nada-ku, Kobe, Hyogo, 657-8501, Japan.

11 <sup>3</sup>Fundamental Particle Physics Laboratory, Graduate School of Science of Nagoya  
12 University, Furocho, Chikusa-ku, Nagoya, Aichi, 464-8602, Japan.

13 <sup>4</sup>Center for Integrated Research and Education of Natural Hazards, Shizuoka  
14 University, 836 Oya, Suruga-ku, Shizuoka City, Shizuoka, Japan.

15 <sup>5</sup>STORY, Ltd., 2-2-5-2321, Minatomachi, Naniwa-ku, Osaka City, Osaka, Japan.

16 *Correspondence to:* Seigo Miyamoto (miyamoto@eri.u-tokyo.ac.jp)

17 **Abstract**

18 One of the key challenges for muographic studies is to reveal the detailed 3D density  
19 structure of a volcano by increasing the number of observation directions. 3D density  
20 imaging by multi-directional muography requires that the individual differences in the  
21 performance of the installed muon detectors are small and that the results from each  
22 detector can be derived without any bias in the data analysis. Here we describe a pilot  
23 muographic study of the Izu–Omuroyama scoria cone in Shizuoka Prefecture, Japan,  
24 from 11 directions, using a new nuclear emulsion detector design optimized for quick  
25 installation in the field. We describe the details of the data analysis and present a  
26 validation of the results.

27 The Izu–Omuroyama scoria cone is an ideal target for the first multi-directional  
28 muographic study, given its expected internal density structure and the topography  
29 around the cone. We optimized the design of the nuclear emulsion detector for rapid  
30 installation at multiple observation sites in the field, and installed these at 11 sites  
31 around the volcano. The images in the developed emulsion films were digitized into  
32 segmented tracks with a high-speed automated readout system. The muon tracks in  
33 each emulsion detector were then reconstructed. After the track selection, including  
34 straightness filtering, the detection efficiency of the muons was estimated. Finally, the  
35 density distributions in 2D angular space were derived for each observation site by  
36 using a muon flux and attenuation models.

37 The observed muon flux was compared with the expected value in the free sky, and is  
38  $88\% \pm 4\%$  in the forward direction and  $92\% \pm 2\%$  in the backward direction. The  
39 density values were validated by comparison with the values obtained from gravity  
40 measurements, and are broadly consistent, except for one site. The excess density at

41 this one site may indicate that the density inside the cone is non-axisymmetric, which  
42 is consistent with a previous geological study.

### 43 **1 Introduction**

44 Scoria or cinder cones are a simple volcanic structure, along with stratovolcanoes,  
45 shield volcanoes, and lava domes. Understanding the internal structure of scoria cones  
46 is important for volcanic hazard assessments. The internal structure of scoria cones  
47 has been mainly investigated by geological approaches. Kereszturi and Németh (2012)  
48 presented a schematic cross-section of typical scoria cones, and Geshi and Neri (2014)  
49 presented detailed photographs of the feeder dike and interior of a scoria cone formed  
50 by the 1809 Etna eruption. Yamamoto (2003) investigated outcrops of the interior of  
51 scoria cones in the Ojika-jima monogenetic volcano group, Nagasaki Prefecture, Japan.  
52 Yamamoto (2003) classified 40 scoria cones according to their degree of interior welding  
53 and proposed a link between lava outflow and cone collapse. However, scoria cones with  
54 such outcrops are rare, and the internal structure can vary markedly among cones.  
55 Therefore, non-destructive methods are required to investigate scoria cones that lack  
56 outcrops.

57 Muography is a non-destructive technique for investigating the internal density  
58 structure of large objects, employing the strong penetrating force of muons, which are  
59 high-energy elementary particles contained in cosmic rays. Muography has also been  
60 used for studying volcanoes, including visualization of a shallow conduit (e.g., Tanaka  
61 et al., 2009), detection of temporal changes in water level due to hydrothermal activity  
62 (Jourde et al., 2016), and 3D density imaging of a lava dome using a joint inversion of  
63 muographic and gravity data (Nishiyama et al., 2017).

64 In unidirectional muography, the only measurable quantity is the density length,  
65 which is the integral of density and length along the muon direction. It has no spatial  
66 resolution along the muon path. Therefore, even if an interesting density contrast is  
67 found below the crater, this could reflect contributions from other parts of the volcanic  
68 body. Similar to X-ray computed tomography, which has been developed as a 3D density  
69 imaging technique, muography can obtain 3D spatial resolution by increasing the  
70 number of observation directions. In previous studies, muography of volcanoes has  
71 been conducted in two or three directions (Tanaka et al., 2010; Rosas-Carbajal et al.,  
72 2017). However, the spatial resolution is not sufficient to determine the detailed  
73 structure of the volcanic interior. Nagahara and Miyamoto (2018) undertook a 3D  
74 density reconstruction based on multi-directional muography and the filtered back-  
75 projection technique. Their study showed that it is necessary to increase the number of  
76 directions to obtain 3D spatial resolution in volcanological studies.

77 Nuclear emulsion is a type of muon detector, and has been used for studies of  
78 volcanoes (Tanaka et al., 2007; Nishiyama et al., 2014; Tioukov et al., 2019). The  
79 trajectories of high-energy charged particles that pass through an emulsion film are  
80 recorded as aligned silver grains with micron-scale resolution (Nakamura et al., 2005;  
81 Tioukov et al., 2019; Nishio et al., 2020). The positions and slopes of aligned grains in a  
82 developed emulsion film are digitized with an automated emulsion readout system  
83 (Kreslo et al., 2008; Morishima and Nakano, 2010; Bozza et al., 2012; Yoshimoto et al.,  
84 2017). Unlike hodoscopes using scintillator bars (e.g., Saracino et al., 2017) or multi-  
85 wire proportional chambers (Olah et al., 2018), a nuclear emulsion film does not have  
86 temporal resolution. In contrast, an emulsion detector does not require electricity,

87 which facilitates the installation of such detectors around volcanoes where the  
88 infrastructure is not well developed.

89 In muographic studies of a volcano, contamination by low-momentum particles must  
90 be removed to derive the correct density (Nishiyama et al., 2014, 2016). Thus, nuclear  
91 emulsion detectors have often been used as an emulsion cloud chamber (ECC), which  
92 comprises alternating layers of films and lead or iron plates (e.g., Kodama et al., 2003).  
93 An ECC detector can measure the momentum of the charged particles, one by one, by  
94 detecting deflection angles caused by multiple Coulomb scattering (Agafonova et al.,  
95 2012). For multiple Coulomb scattering, there is a relationship between the maximum  
96 detectable momentum  $p_{max}$  and position resolution  $y_{reso}$  as follows using the first term  
97 of Eq. (33.16), and (33.20) in Tanahashi et al., (2018):

$$98 \quad p_{max} \sim \alpha X_0^{-0.5} x^{1.5} y_{reso}^{-1} \quad (1)$$

99 where  $\alpha$  is a constant,  $X_0$  is the radiation length of a material, and  $x$  is the thickness of  
100 the material. The position resolution of the newest scintillator hodoscope or MWPC is  
101 on the order of 1 mm (Saracino et al., 2017; Olah et al., 2018). In the case of nuclear  
102 emulsion, the resolution is about 1  $\mu\text{m}$ . When using ECC, the thickness of the material  
103 can be reduced to 1/100 while maintaining the same  $p_{max}$ , which is advantageous in  
104 terms of transportation in the field.

105 A new design of the ECC detector was also required for its rapid installation at  
106 multiple observation sites in the field. In a previous study of volcano observations  
107 using the ECC detector (Nishiyama et al., 2014), rapid installation of the detector was  
108 not required because the number of observation sites was just one. It is also important  
109 to establish a data analysis procedure for the muon tracks recorded by the ECC  
110 detectors. To derive an accurate density value for the volcanic body, it is necessary to

111 remove low-momentum contamination, estimate the detection efficiency, and validate  
112 the results. In addition, for bias-free 3D imaging by multi-directional muography, the  
113 installed muon detectors must show similar performance.

## 114 **2 Izu–Omuroyama scoria cone**

115 The Izu–Omuroyama scoria cone (34°54'11"N, 139°05'40"E; 580 m a.s.l.) is one of the  
116 largest scoria cones in the world, and is part of the Higashi Izu monogenetic volcano  
117 group (Aramaki and Hamuro, 1977), which is located in the northeastern Izu  
118 Peninsula, Ito City, Shizuoka Prefecture, Japan. It is considered to have formed about  
119 4,000 years ago, based on <sup>14</sup>C dating (Saito et al., 2003). The basal diameter is 1,000 m,  
120 the height is 280 m from the base, and the typical slope of its flanks are 29–32°. The  
121 center of the cone contains a crater that is 250 m wide and 40 m deep. The volume of  
122 the cone is  $71 \times 10^6 \text{ m}^3$ , and lava with a volume of  $\sim 10^8 \text{ m}^3$  has flowed out from the  
123 base of the cone (Koyano et al., 1996). The lava is a basaltic andesite with 54–56 wt.%  
124 SiO<sub>2</sub> (Hamuro, 1985).

125 Although the shape of the Izu–Omuroyama scoria cone appears to be axisymmetric  
126 (Fig. 1), a geological study suggested it has an anisotropic structure due to the  
127 following reasons. (i) During/after the growth of the cone, some interior parts became  
128 welded due to loading, residual heat, and a low cooling rate. As a result, some denser  
129 material formed. (ii) At the end of the eruption, a lava lake was formed in the crater,  
130 and the lava flowed out to the western foot of the cone. (iii) There is a small crater on  
131 the south side of the cone, which is thought to have formed when the main crater was  
132 blocked at the end of the eruption (Koyano et al., 1996).

133 The bulk density of typical continental crust is about  $2.6\text{--}2.7 \times 10^3 \text{ kg m}^{-3}$ . The bulk  
134 densities reported for scoria deposits are  $0.84\text{--}1.01 \times 10^3 \text{ kg m}^{-3}$  (Taha and Mohamed,  
135 2013) and  $0.56\text{--}1.20 \times 10^3 \text{ kg m}^{-3}$  (Bush, 2001). Therefore, the maximum expected  
136 density contrast is about  $1.4\text{--}2.0 \times 10^3 \text{ kg m}^{-3}$ , due to the difference in porosity  
137 between welded rocks and scoria deposits. In addition, the Izu–Omuroyama scoria cone  
138 is an ideal target for multi-directional muography due to the accessibility to detector  
139 sites and absence of muographic shadows from any direction caused by other  
140 topographic features.

141



142 Figure 1. Photograph of the Izu–Omuroyama scoria cone from the northwest, taken by  
143 an unmanned aerial vehicle (Koyama, 2017).  
144

### 145 3 Multi-directional muography observations using emulsion cloud chambers

#### 146 3.1 Detector design

147 Emulsion films were manufactured by pouring 70  $\mu\text{m}$  of nuclear emulsion on both  
148 sides of a 180  $\mu\text{m}$ -thick plastic base. The size of a film is 125  $\times$  100 mm. The films were  
149 vacuum-packed in a light-blocking envelope to maintain their planar form, which  
150 prevented air bubbles forming between the envelope and film, and made it easy to  
151 handle the films in the field.

152 The detector used for the 2018 observations is basically the same as that of Nishiyama  
153 et al. (2014), and only the number of lead plates was different. The former consists of  
154 20 films and 9 plates of 1-mm-thick lead, the latter consists of 20 films and 19 lead  
155 plates. At the time of installation in 2018, the films, lead plates, and supports were all  
156 in pieces and, therefore, a lot of time and effort was required for assembly in the field.  
157 The more efficient detector design was required for rapid and error-free installation.

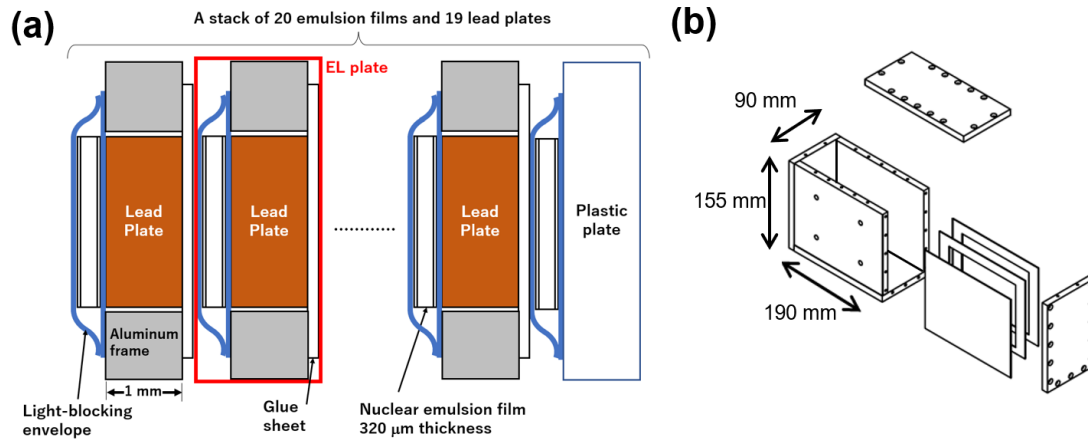
158 The detector used in the 2019 observations was improved. It consists of an ECC and  
159 an outer box. The ECC consists of 20 emulsion films and 19 lead plates, each 1 mm  
160 thick (Fig. 2a). An aluminum frame was fixed to a lead plate with a thin sheet of glue,  
161 and then an emulsion film with the light-blocking envelope was attached with scotch  
162 tape. In this paper, we term this unit the emulsion–lead plate (EL plate; Fig. 2a). The  
163 EL plate was designed for quick assembly in the field.

164 The outer box consists of 10-mm-thick aluminum plates (Fig. 2b). The outer size of  
165 this box is 190 mm in width, 155 mm in height, and 90 mm in depth. An ECC and  
166 strong springs were placed in the box. There are four screw holes on one side of the box,  
167 and by turning the bolts and pushing the spring plate, a uniform pressure ( $\sim 10^5$  Pa)

168 was applied to the ECC. This pressure prevents the film from stretching and shrinking  
169 due to temperature changes.

170 Given that there is no temporal resolution in emulsion films, ordinary ECC detectors  
171 cannot distinguish whether cosmic-ray tracks pass the ECC during muographic  
172 observation or transportation and standby. Thus, we also added a similar gimmick as  
173 previous muographic studies using emulsion films as previous muographic studies  
174 using emulsion films. The researchers have been used emulsion films with a different  
175 alignment during the muon observations and standby (e.g., Tanaka et al., 2007). In the  
176 present study, the corners of the EL plates were aligned during the muon observations,  
177 while the corners were intentionally shifted a few millimeters horizontally and fixed  
178 with clamps during standby (Fig. 3). This alignment difference distinguishes passing  
179 charged particles during non-observation and observation periods by pattern matching  
180 of each emulsion film. By using this procedure, the time to set the alignment between  
181 each EL plate in the field is <30 s. Although the muon tracks that pass through an  
182 ECC during the alignment set-up may become noise, our procedure reduced such  
183 tracks.

184

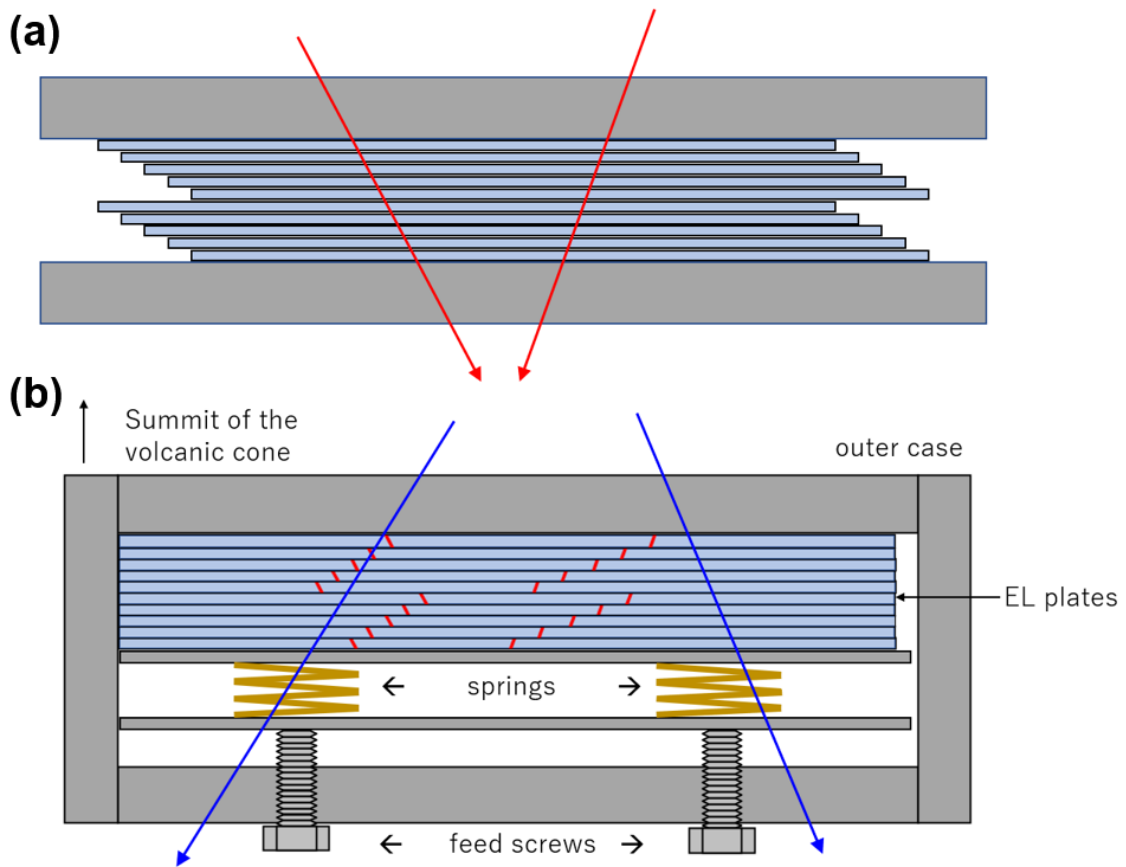


185

186 Figure 2. Design of the ECC and outer box. (a) Schematic cross-section of the EL plates  
 187 and an ECC. The EL plate consists of a 1-mm-thick aluminum frame, 1-mm-thick lead  
 188 plate, 100- $\mu\text{m}$ -thick glue sheet that fixes a lead plate to an aluminum frame, and an  
 189 emulsion film with a light-blocking envelope. An ECC consists of 19 EL plates and an  
 190 emulsion film with a plastic plate. (b) Schematic of the aluminum outer box. The  
 191 thickness of the aluminum plate is 10 mm. The ECC shown in (a) was set inside this  
 192 box. There are four holes for feed screws in the front plate.

193

194



195

196

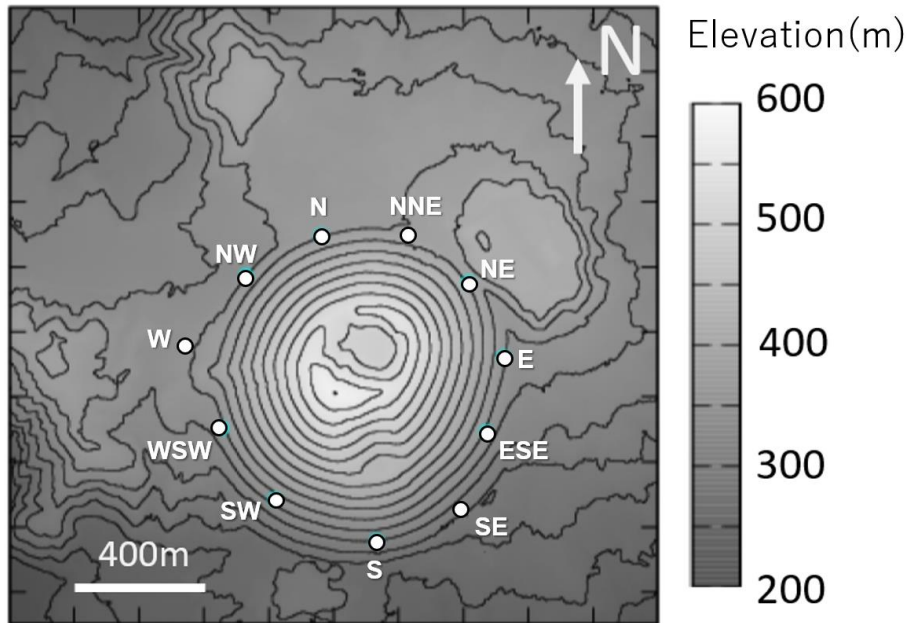
197 Figure 3. (a) View of the EL plates from above during standby. The EL plates were  
198 intentionally shifted a few millimeters horizontally and fixed with a pair of steel plates  
199 and clamp. The red lines represent the muon tracks in this alignment. (b) View from  
200 above during the observations. The EL plates were aligned to the side of the outer box,  
201 and fixed by the springs and feed screws. The blue lines represent muon tracks during  
202 observations. Note that the red tracks cannot be reconstructed in this alignment.

203

204 **3.2 Installation**

205 The detectors were installed at three sites in 2018 and eight sites in 2019 around the  
206 Izu–Omuroyama scoria cone (Fig. 4; Table 1). Each detector was buried in a hole that  
207 was about 40 cm deep to avoid high temperatures due to direct sunlight. This is done  
208 because the number of latent image specks decreases, and the number of randomly  
209 generated specks increases, under high-temperature conditions (Nishio et al., 2020).  
210

211



212

213

214 Figure 4. Topography of the Izu–Omuroyama scoria cone. White dots represent  
215 observation sites.

216

Detector site ID	Effective area (cm <sup>2</sup> )	Exposure time (days)
W, SE, and NNE (2018)	120	60
N, NW, WSW, SW, S, ESE, E, and NE (2019)	240	90

217 Table 1. Effective area and muon exposure time for each detector.

218

219

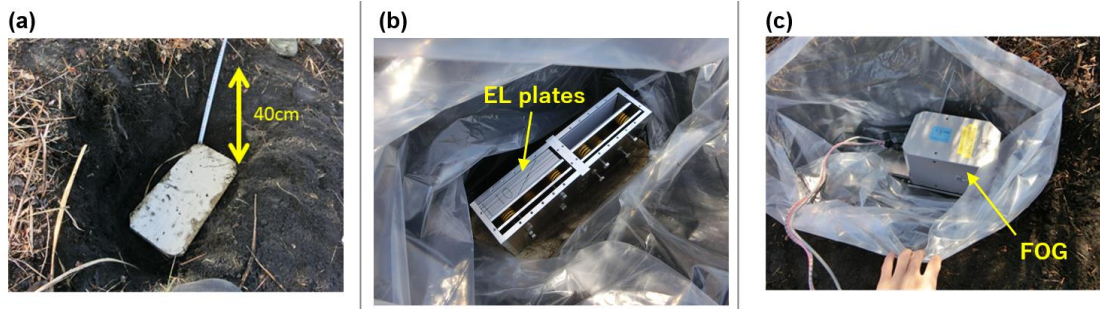
220 The installation procedure at each observation site in 2019 was as follows (Fig. 5).

- 221 1) Carry the outer box and EL plates to the observation site.
- 222 2) Measure the coordinates of the site with a hand-held GPS (GERMIN; model GPS  
223 eTrex 30J). The typical uncertainty of the latitudinal and longitudinal coordinates  
224 is 3 m.
- 225 3) Dig a hole in the ground with horizontal dimensions of  $60 \times 40$  cm and a depth of  
226 40 cm.
- 227 4) Flatten the base of the hole, place a plastic bag inside the hole, and lay down a  
228 piece of plywood.
- 229 5) Put double-sided tape on the bottom of the outer box and place it on the plywood.
- 230 6) Put the stack of EL plates into the box and quickly align these ( $<30$  s).
- 231 7) Close the cap of the outer box.
- 232 8) Turn the feed screws to increase the pressure.
- 233 9) Measure the attitude of the outer box (i.e., the yaw [absolute azimuth angle], roll,  
234 and pitch). The yaw was measured with a fiber optic gyro (Japan Aviation  
235 Electronics Industry Ltd.; model FOG JM7711; Watanabe et al., 2000), and the roll  
236 and pitch were measured by the digital leveler. The typical errors on the yaw, roll,  
237 and pitch are  $8.7 \times 10^{-3}$ ,  $1.0 \times 10^{-3}$ , and  $1.0 \times 10^{-3}$  radians, respectively.
- 238 10) Cover with styrofoam to avoid heating from the ground surface.
- 239 11) Close the plastic bag to keep water out.
- 240 12) Backfill the hole.

241

242 The time taken for this installation was ~2 h for each site, and we installed detectors  
243 as three sites in a day in 2019. The detector retrieval procedure was the opposite of the  
244 installation procedure. The 380 films were developed in a darkroom. The deposited  
245 silver particles on the surface of the films were removed with anhydrous ethanol. The  
246 gelatin of the sensitive layer was swollen with a glycerin solution to obtain the  
247 optimum thickness for an automated track readout system, which is described in the  
248 next section.  
249

250



251

252

253 Figure 5. Photographs showing the installation procedure. (a) Dig a hole and place a  
254 plywood sheet in the bottom. (b) Place the outer box in the hole and put a stack of EL  
255 plates into the box. The plates were aligned over a period of <30 s. After closing the top  
256 plate of the box, the feed screws were tightened to increase the pressure. (c) The yaw,  
257 roll, and pitch were measured with a fiber optic gyro (FOG) and digital leveler.

258

## 259 **4 Track reconstruction, selection, and detection efficiency estimation**

### 260 **4.1 Track reconstruction**

261 A track of a high-energy charged particle is recorded as an aligned line of silver grains  
262 in the emulsion film (e.g., Nakamura et al., 2005). The images in the 380 nuclear  
263 emulsion films were scanned and the positions and slopes of the tracks were digitized  
264 by “HTS”, which is a high-speed automated track readout system at Nagoya University  
265 (Yoshimoto et al., 2017). For each ECC, the tracks of the charged particles were  
266 digitally reconstructed from the segmented tracks in 20 films. NETSCAN 2.0 software  
267 was used for track reconstruction (Hamada et al., 2012). NETSCAN 2.0 rapidly  
268 corrects for film distortions and local misalignments between films by using many  
269 tracks recorded over a large area. It then outputs all possible connections as the final  
270 result. NETSCAN 2.0 has been used in various fields, such as neutrino physics  
271 (Hiramoto et al., 2020), cosmic ray astronomy (Takahashi et al., 2015), and muographic  
272 studies of Egyptian pyramids (Morishima et al., 2017). The typical procedure for the  
273 track reconstruction is as follows.

274

- 275 1) Reconstruct the “base track”, which is connected between the emulsion layers  
276 across the plastic base of 170  $\mu\text{m}$  in a film.
- 277 2) Reconstruction of the “linklet”, which is the base track pair between adjacent films  
278 across lead plates.
- 279 3) Reconstruction of the tracks that connect across the whole ECC. If no base track  
280 was found in two consecutive films on the extension of a track, then the track was  
281 considered to have stopped.

282

283 For example, in  $ECC\_ID = 02$ ,  $8.9 \times 10^6$  base tracks,  $3.2 \times 10^6$  linklets in a pair of  
284 adjacent films, and  $1.7 \times 10^7$  tracks in an entire ECC were reconstructed.

## 285 4.2 Track selection

286 NETSCAN 2.0 outputs all possible track connections. Therefore, it is necessary to  
287 carefully select the tracks for the muographic analysis. A schematic example of the  
288 output tracks is shown in Fig. 6. Most of the branches can be considered to represent  
289 contamination by fake base tracks caused by random noise, or the coincidental  
290 occurrence of low-energy positrons/electrons on parallel slopes in the vicinity of the real  
291 tracks (e.g., Fig. 6; cases 2 and 3). For reference, the position dependence of noise  
292 density is described in Appendix A. Some branches consist of a pair of straight tracks  
293 with small closest distances and similar angles (Fig. 6; case 4). In this case, the two  
294 tracks should be separated.

295 The following  $\chi^2/ndf$  value was calculated for all tracks for the low momentum cut-  
296 off:

$$297 \quad \chi^2/ndf = \sum_m \left[ \left( \frac{\Delta\theta_R^m}{\sigma_R^m} \right)^2 + \left( \frac{\Delta\theta_L^m}{\sigma_L^m} \right)^2 \right] / ndf \quad (2)$$

298 where  $ndf$  is the number of degrees of freedom and  $m$  is the index of adjacent film pairs  
299 (i.e., [1,2], [2,3], [3,4], ..., and [18,19], [19,20] in Fig. 6) or with one skip if there was a  
300 base track inefficiency (i.e., [1,3], [2,4], [3,5], ..., [17,19], [18,20]).  $\Delta\theta_R^m =$   
301  $(\Delta\theta_x^m \times \tan\theta_x + \Delta\theta_y^m \times \tan\theta_y) / \sqrt{\tan^2\theta_x + \tan^2\theta_y}$  and  $\Delta\theta_L^m = (\Delta\theta_y^m \times \tan\theta_x -$   
302  $\Delta\theta_x^m \times \tan\theta_y) / \sqrt{\tan^2\theta_x + \tan^2\theta_y}$ , and  $\Delta\theta_x^m$  and  $\Delta\theta_y^m$  are angular differences along the  
303  $x, y$  coordinates of the ECC.  $\sigma_R^m$  and  $\sigma_L^m$  are the root-mean-square of  $\Delta\theta_R^m$  and  $\Delta\theta_L^m$ ,

304 which were calculated for every adjacent film pair in every ECC (Fig. 7). Figure 8

305 shows the distribution of  $\chi^2/ndf$  for all tracks in an ECC.

306 The procedure for track selection is as follows.

307 1) Select tracks that start from one of the two most upstream (i.e., summit cone side)

308 films and stop at one of the two most downstream films.

309 2) Select tracks with  $\chi^2/ndf < 5.0$ .

310 3) If a track has any branches, then:

311 a) If the shared proportion of track length is  $\geq 20\%$ , choose the longest branch. If

312 the track lengths are the same, then choose the branch with the smallest

313  $\chi^2/ndf$ .

314 b) If the shared proportion of track length is  $< 20\%$  (Fig. 6; case 4), then the

315 branches were divided into two tracks.

316 We estimated the effect of the straightness filtering using  $\chi^2/ndf < 5.0$ . Figure 9 shows

317 the momentum filtering efficiency. This figure was derived from a simple simulation in

318 which the interaction of charged particles inside the ECC was assumed to be multiple

319 Coulomb scattering only, and the scattering angle was approximated by a Gaussian

320 distribution. The path length in the lead plates becomes longer when the track has a

321 larger slope, and thus the momentum also becomes higher. Based on the background

322 noise study by Nishiyama et al. (2016), the size of the mountain body used in the

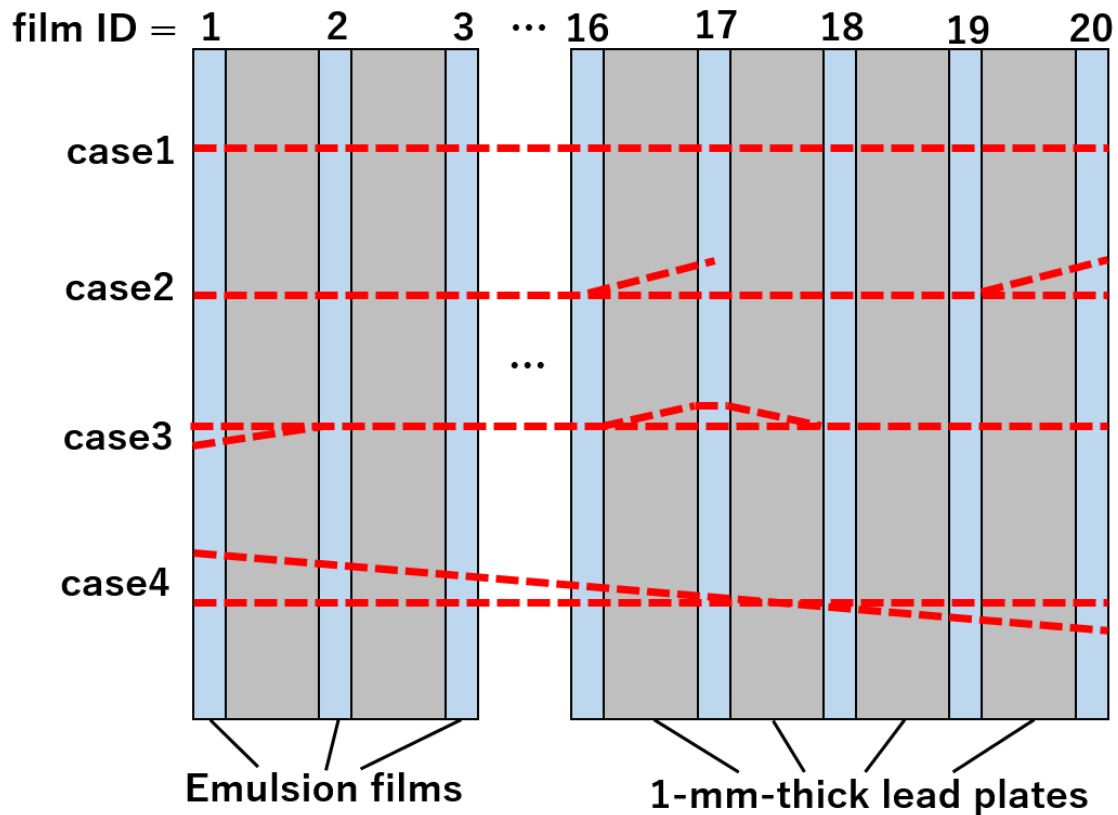
323 simulation and the Izu–Omuroyama scoria cone is broadly the same, and thus the

324 rejection efficiency should be sufficient. For example, after the track selection,

325  $1.7 \times 10^6$  tracks were selected at the site “N”.

326

327



329

330

331 Figure 6. Schematic examples of typical reconstructed tracks in an ECC obtained by  
 332 NETSCAN 2.0. Upstream means towards the volcanic cone side and downstream  
 333 means the backward free sky direction.

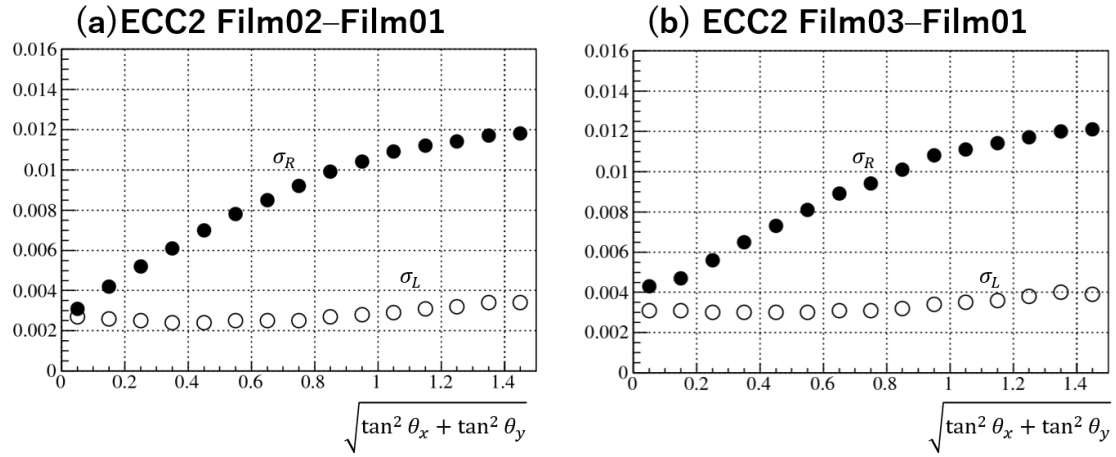
334 Case 1: a straight track without any branches.

335 Case 2: a straight track with a branch in the middle and downstream films. The track  
 336 branch in the middle was rejected by selection step (1). The branch in the most  
 337 downstream film was merged into the straight track by selection step 3a.

338 Case 3: branches in the upstream and middle films. Both branches were merged into a  
 339 straight track by selection step 3a.

340 Case 4: a pair of straight tracks with small closest distances and similar angles. If the

341 shared proportion of the track length was <20%, the tracks were divided into two  
342 different tracks by selection step 3b.  
343

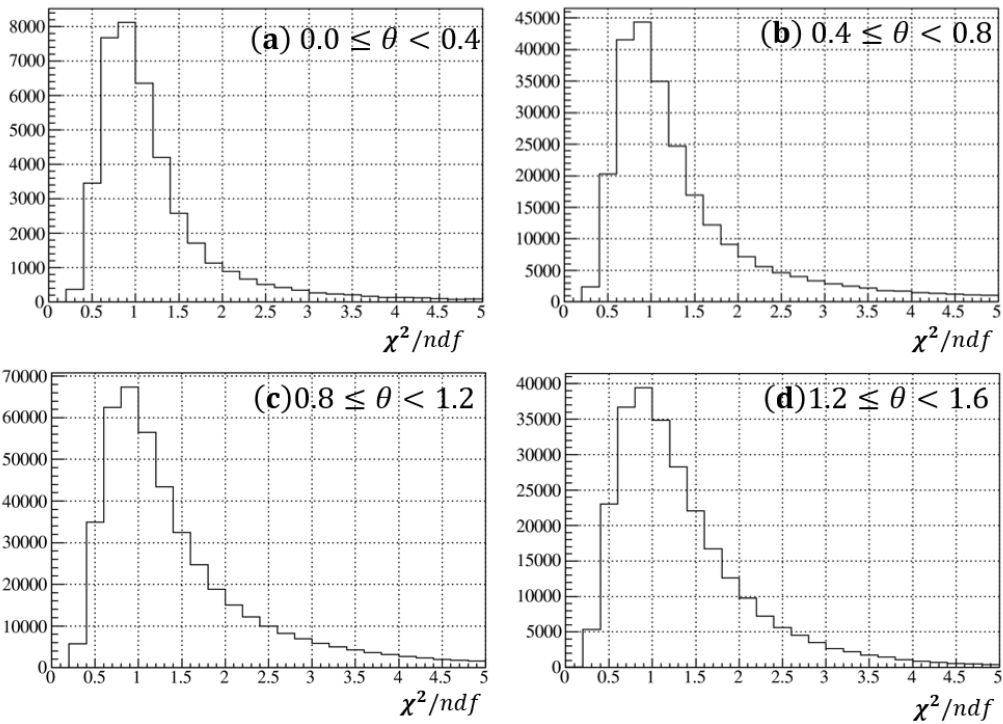


344

345 Figure 7. Examples of  $\sigma_R$  and  $\sigma_L$  as a function of  $\sqrt{\tan^2 \theta_x + \tan^2 \theta_y}$ . The values were

346 determined by the ECC and used to calculate the value of Eq. (2).

347

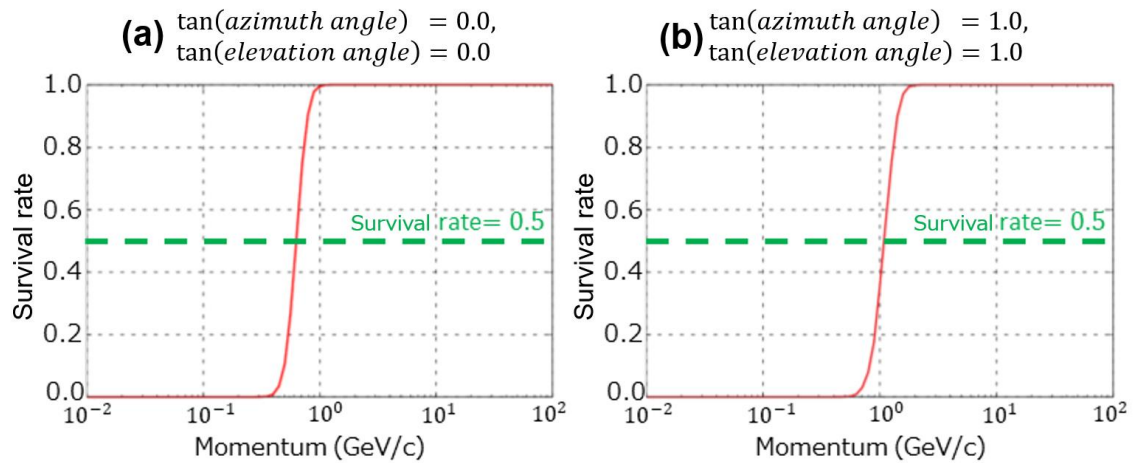


348

349 Figure 8. Example of the  $\chi^2/ndf$  distribution for selected tracks as a function of  $\theta =$

350  $\sqrt{\tan^2 \theta_x + \tan^2 \theta_y}$  in an ECC. (a)  $0 \leq \theta < 0.4$ , (b)  $0.4 \leq \theta < 0.8$ , (c)  $0.8 \leq \theta < 1.2$ , and (d)

351  $1.2 \leq \theta < 1.6$ .



352

353 Figure 9. Survival rate of muons after the straightness cut-off as a function of

354 momentum. (a) Track angles with  $\tan(\text{relative azimuth}) = 0.0$  and

355  $\tan(\text{elevation angle}) = 0.0$ . (b) Track angles with  $\tan(\text{relative azimuth}) = 1.0$  and

356  $\tan(\text{elevation angle}) = 1.0$ . The path length in the lead plates becomes longer when the

357 track has a larger slope, and thus the remaining momentum also becomes higher for

358 the latter case. The momentum values at a survival rate of 0.5 are 0.6 and 1.1 GeV/c,

359 respectively.

360

361 **4.3 Detection efficiency estimation**

362 The muon detection efficiency can be estimated by investigating the percentage of  
 363 tracks that have a base track in a film. In this paper, we term this percentage the “fill  
 364 factor”. The fill factor  $\varepsilon$  can be defined as follows:

$$365 \quad \varepsilon_j(\theta_x, \theta_y) = \frac{N_j(\theta_x, \theta_y)}{N_{j-1, j+1}(\theta_x, \theta_y)} \quad (3)$$

366 where  $j$  is a film ID,  $N_{j-1, j+1}(\theta_x, \theta_y)$  is the number of tracks in which base tracks were  
 367 found in films  $j - 1$  and  $j + 1$ , and  $N_j(\theta_x, \theta_y)$  is the number of tracks in which base  
 368 tracks were found in films  $j - 1, j$ , and  $j + 1$ . The fill factor depends on the films and  
 369 track slopes  $\theta_x$  and  $\theta_y$ . The position dependence of the fill factor is described in  
 370 Appendix A.

371 Using the fill factor  $\varepsilon_j(\theta_x, \theta_y)$  and  $\bar{\varepsilon}_j(\theta_x, \theta_y) = 1 - \varepsilon_j(\theta_x, \theta_y)$ , the muon detection  
 372 efficiency  $\epsilon$  in an ECC can be calculated as follows:

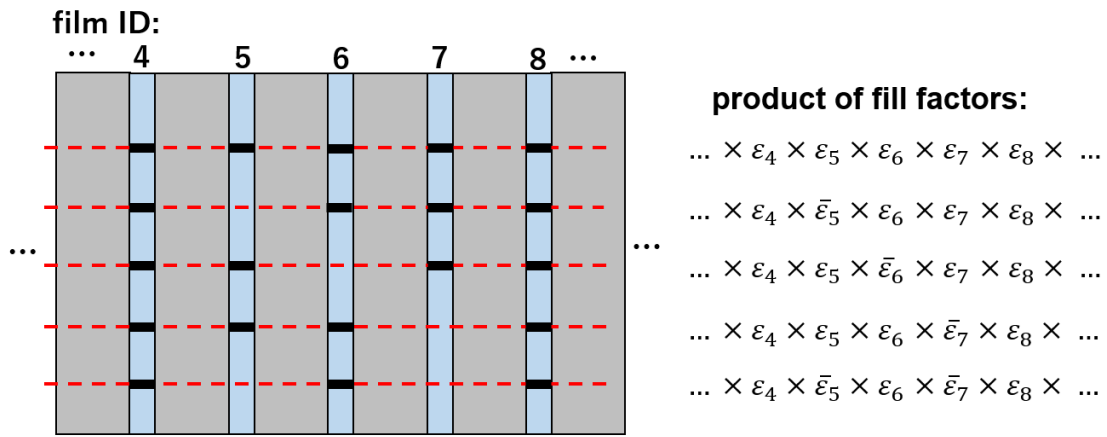
$$373 \quad \epsilon(\theta_x, \theta_y) = \sum_{hit\ pattern} \varepsilon_1 \times \bar{\varepsilon}_2 \times \varepsilon_3 \times \dots \times \bar{\varepsilon}_{18} \times \varepsilon_{19} \times \varepsilon_{20} \quad (4)$$

374 where *hit pattern* is the summation for all possible hit patterns (e.g.,  $\varepsilon_1 \times \bar{\varepsilon}_2 \times \varepsilon_3 \times$   
 375  $\dots \times \bar{\varepsilon}_{18} \times \varepsilon_{19} \times \varepsilon_{20}$  or  $\bar{\varepsilon}_1 \times \varepsilon_2 \times \varepsilon_3 \times \dots \times \varepsilon_{18} \times \bar{\varepsilon}_{19} \times \varepsilon_{20}$ ) from the track selection  
 376 conditions described in section 4.2 (Fig. 10). An example of the angular distribution of  
 377 the fill factor  $\varepsilon_j(\theta_x, \theta_y)$  and muon detection efficiency  $\epsilon(\theta_x, \theta_y)$  in an ECC is shown in  
 378 Fig. 11. The statistics of observed muons were limited in some angular bins by the  
 379 thick volcanic cone. However, the statistics were sufficient in the backward region (i.e.,  
 380 elevation angle  $< 0.0$ ). We used the distribution of the negative elevation angular  
 381 region instead of the positive region, because it has enough statistics and the optics of  
 382 the HTS has an approximately two-fold rotational symmetry.

383

384

385

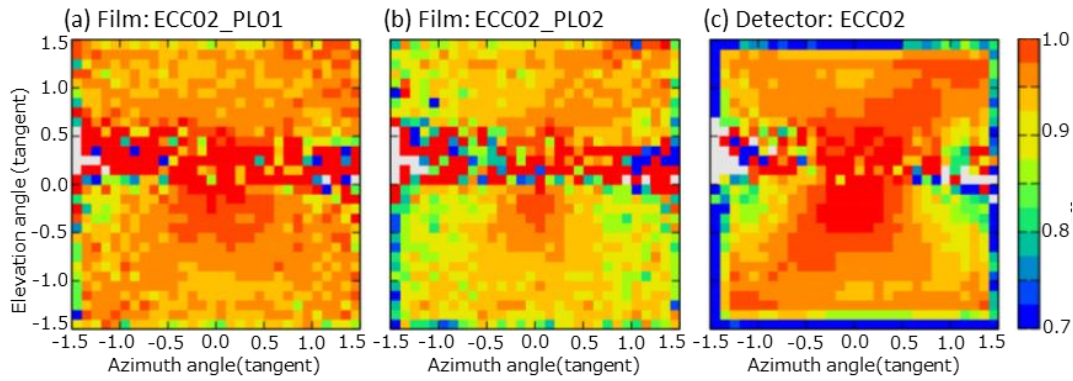


386

387 Figure 10. Example of all hit patterns and the products of fill factors in Eq. (4) when  
 388 base tracks are found in film ID numbers 4 and 8. The red lines indicate the  
 389 reconstructed tracks and the short black lines represent the base tracks found in the  
 390 films.

391

392



393

394 Figure 11. Examples of the angular distribution of the fill factor in some films and the  
395 efficiency of an ECC. (a) Fill factor for film ID = PL01 (most upstream film) and ECC  
396 ID = 02 at site “N”. (b) Fill factor for film ID = PL02 and ECC ID = 02. (c) Muon  
397 detection efficiency for ECC ID = 02 as evaluated by Eq. (4). The horizontal axis is the  
398 tangent of azimuth angle; the vertical axis is the tangent of the elevation angle; the  
399 colors represent the fill factor/efficiency values. A positive elevation angle means the  
400 muon path is from the cone; a negative elevation angle means the muon path is from  
401 the backward free sky. The gray color means there were no observed muons in the  
402 angular bin due to the thick volcanic cone.

403

404 **5 Results**

405 The average density along muon path was determined for each observation site. We  
 406 used the muon flux model of Honda et al. (2004), energy loss model of Groom et al.  
 407 (2001), and topography around the Izu–Omuroyama scoria cone from the Geospatial  
 408 Information Authority of Japan (<https://maps.gsi.go.jp/>). The coordinates of the  
 409 observation site, direction, sensitive area, thickness of the ECC detectors, and  
 410 observation time were used to calculate the expected number of muons at each  
 411 observation site. The expected number of muons can be calculated as a function of the  
 412 average density  $\rho_k$  along the path:

413 
$$N_k^{simu}(\rho_k) = f_k(\rho_k, L_k) \times S_k \times \Omega_k \times T \times \epsilon_k \quad (5)$$

414 where  $k$  is the index of an angular bin,  $f_k(\rho_k, L_k)$  is the penetrating muon flux  
 415 (calculated from the muon flux model, energy loss model, and path length  $L_k$ ),  $S_k$  is the  
 416 sensitive area of the ECC,  $\Omega_k$  is the solid angle,  $\epsilon_k$  is the muon detection efficiency, and  
 417  $T$  is the observation time.

418 The angular bin size used for calculating the expected value was  $(0.01)^2$  in terms of  
 419 the tangent. The angular bins were then merged to improve the statistical accuracy of  
 420 the observed values. This merging procedure is useful in topology where a small  
 421 change in elevation angle can dramatically change the path length in the volcano. If  $k$   
 422 is the index of the angular bins of  $(0.01)^2$  and the bins belong to a larger angular bin  $i$ ,  
 423 then the following equation holds:

424 
$$N_i^{merged}(\rho_i) = \sum_k N_k^{simu}(\rho_i) \quad (6)$$

425 where  $\rho_i$  is the density of the merged angular bin  $i$ . If  $N_i^{obs}$  is the number of the  
 426 detected muons in the angular bin  $i$ , then we can uniquely determine the density value

427  $\rho_i$ , such that  $N_i^{merged}(\rho_i) = N_i^{obs}$ . The lower limit  $\rho_i^{low}$  and upper limit  $\rho_i^{up}$  caused by the  
 428 statistical error on  $N_i^{obs}$  can also be estimated as follows:

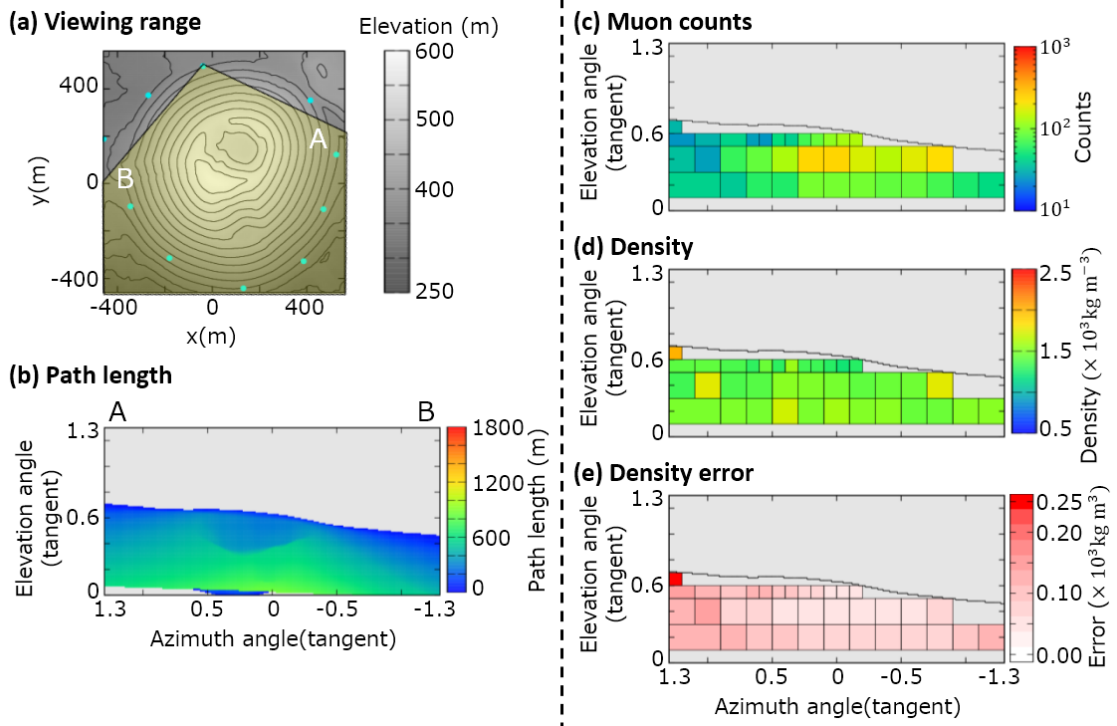
$$429 \quad N_i^{merged}(\rho_i^{low}) = N_i^{obs} + \sqrt{N_i^{obs}} \quad (7)$$

$$430 \quad N_i^{merged}(\rho_i^{up}) = N_i^{obs} - \sqrt{N_i^{obs}} \quad (8)$$

431 An example of the derived density map is shown in Fig. 12. All results are shown in  
 432 Figs 17–26 (Appendix B).

433 The definition of the angular bin areas was based on the following. The size of the  
 434 angular bins was  $(0.2)^2$  when the elevation angle is 0.1 to 0.5 in tangent terms. When  
 435 the elevation angle is  $>0.5$ , the angular bin size was  $(0.1)^2$ . If the observed muon count  
 436 in the bin was  $<25$ , the angular bin was manually merged with adjacent bins to  
 437 improve the statistical error. The angular bin with a near-surface path (path length  $<$   
 438 30 m) was excluded to avoid ambiguity between the actual topography and digital  
 439 elevation map. The attitude errors of each muon detector also contribute to the path  
 440 length ambiguity, especially near the surface of the cone.

441



443

444

445 Figure 12. Data for observation site N. (a) Map, topography, and viewing range; (b)  
 446 path length of the volcanic cone; (c) muon counts  $N_i^{obs}$ ; (d) density  $\rho_i$ . The maximum  
 447 value of the color bar indicates a density of  $>2.5 \times 10^3 \text{ kg m}^{-3}$  and the minimum value  
 448 is  $<0.5 \times 10^3 \text{ kg m}^{-3}$ . (e) Density error  $\Delta\rho = (\rho_i^{up} - \rho_i^{low})/2$ . The maximum value of the  
 449 color bar indicates a density error of  $>0.25 \times 10^3 \text{ kg m}^{-3}$ .

450

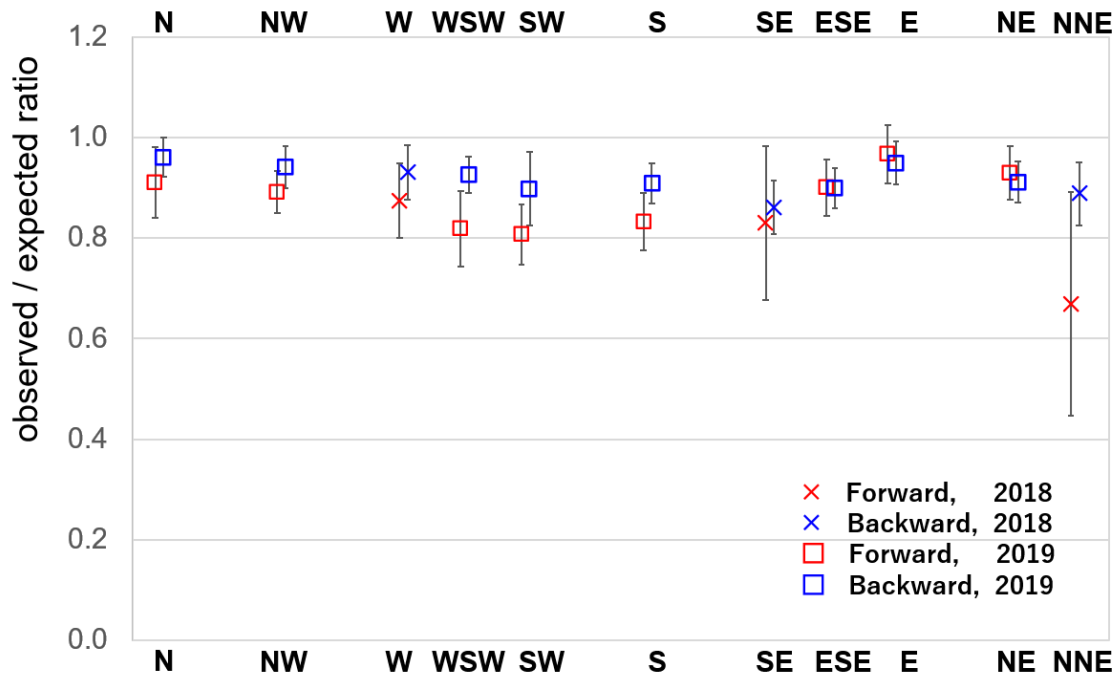
## 451 6 Validation

452 Firstly, we validated the observed muon flux by comparing it with the muon flux  
453 model in the free sky region. The average and standard deviation of the ratio between  
454 the sites were  $88\% \pm 4\%$  in the forward direction and  $92\% \pm 2\%$  in the backward  
455 direction, except for the NNE site (Fig. 13). An example of observed/expected muon flux  
456 ratio angular distribution of the site N is shown in Fig. 14. As can be seen in this  
457 figure, in each detector site, the ununiform distribution of the observed/expected muon  
458 flux ratio exists. Such deviations were 4%–7% except the forward directions at the site  
459 SE and NNE. For reference, a 10% error on the flux corresponds to a 4% error on the  
460 density length at a  $\tan(\text{elevation angle}) = 0.2$  and density length = 1000 m (water  
461 equivalent). These deviations were less than the errors caused by the muon statistics.  
462 The discrepancy for the NNE site is discusses in the next section.

463 Secondly, we compared the density of the entire volcanic cone determined by gravity  
464 data with that obtained by muography. Table 2 shows the density determined from  
465 each observation site when the cone is assumed to be uniform. The calculation of the  
466 overall density  $\bar{\rho}$  is as follows:

$$467 \quad \bar{\rho} = \frac{\sum_i \rho_i V_i}{\sum_i V_i} \quad (9)$$

468 where  $i$  is the index of the angular bins and  $V_i$  is the volume of the volcanic cone cut off  
469 by the angle bin  $i$ . Based on the gravity study of Nishiyama et al. (2021), the density of  
470 the Izu–Omuroyama scoria cone is  $1.39 \pm 0.07 \times 10^3 \text{ kg m}^{-3}$ . The overall density  
471 derived by muography at each observation site is  $1.42\text{--}1.53 \times 10^3 \text{ kg m}^{-3}$ , except for  
472 one site. These values are broadly consistent with the density determined from gravity  
473 data, except for the observation site W ( $1.72 \times 10^3 \text{ kg m}^{-3}$ ).

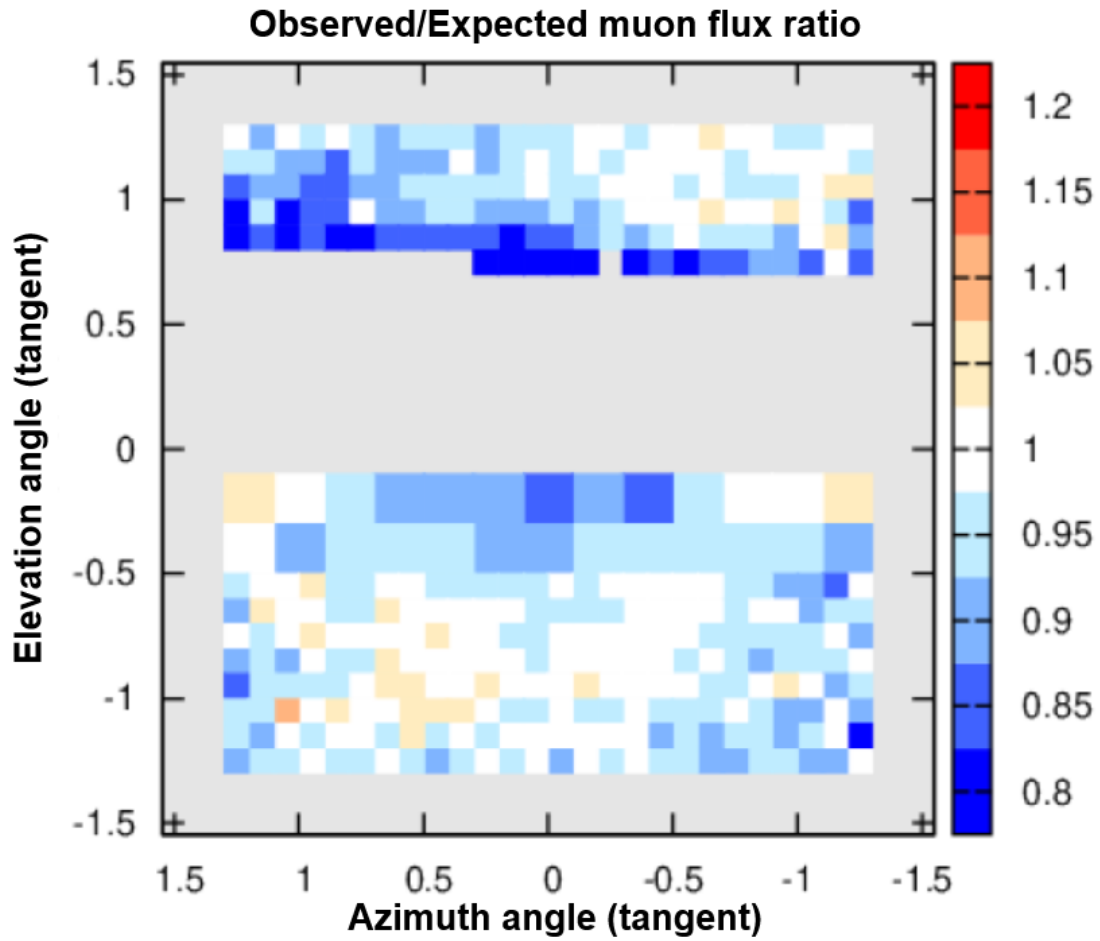


474

475 Figure 13. The observed/expected muon flux ratio for each observation site in the  
 476 free sky region. The plot represents the average value of the ratio in tangential  
 477 angular space, and the error bars are the standard deviations at each site.

478

479



480

481

482 Figure 14. Example of the observed/expected muon flux ratio in the free sky region at

483 site N. The horizontal axis represents azimuth angle, and the vertical axis represents

484 the elevation angle. Positive elevation angle means the muons come from forward

485 directions (the volcanic cone). Negative elevation angle means the muons come from

486 backward free sky directions. Typical deviation of the ratio is 4%–7% in each site.

487

488

489

Observation site	Overall density $\bar{\rho}$ ( $\times 10^3$ kg m $^{-3}$ )	Observation site	Overall density $\bar{\rho}$ ( $\times 10^3$ kg m $^{-3}$ )
N	1.51	S	1.49
NW	1.45	ESE	1.45
W	1.72	E	1.42
WSW	1.50	NE	1.53
SE	1.46	NNE	1.50
SW	1.48		

490 Table 2. Overall bulk density obtained by muography, assuming that the density is

491 uniform in the volcanic cone.

492

493 **7 Discussion**

494 For the observed/expected muon flux ratio in the free sky region, the values in the  
495 forward direction are less than in the backward direction at many observation sites.  
496 This could be because the detectors were buried in holes on steep slopes ( $\sim 30^\circ$ ), and our  
497 analysis might not account for that effect. Due to the steep slope, muons arriving from  
498 the forward direction need to penetrate some amount of soil, whereas muons from the  
499 backward direction can enter the detector without being affected by the soil cover. In  
500 addition, the resolution of the detector coordinates is  $\sim 3$  m, which might also contribute  
501 to the discrepancy.

502 Some density results from near the ground surface are complex. Some regions near the  
503 path length of 30 m appear to have relatively higher or lower density than the other  
504 data (e.g., Fig. 22, 25). One possible reason for this is the error on the detector attitude.  
505 Near the surface of the volcanic cone, the difference between the calculated and actual  
506 path lengths may become larger due to the error on the detector attitude.

507 The anomalous data for the NNE site also warrants further consideration. The reason  
508 for this might be a difference between the digital elevation map and actual topography.  
509 There is a stone wall in front of the buried detector at this site, which is about 1 m high  
510 and located on the volcanic cone side. The grid size of the digital elevation map used in  
511 this study is 1 m, and thus the map might not record this steep gradient.

512 In summary, errors in the position and attitude of the detectors, and the accuracy of  
513 the DEM, might cause a misfit between the DEM and actual topography. These are the  
514 main reasons for the discrepancy between the observed and expected muon flux.

515 The discrepancy between the observed and expected muon flux was  $\pm 4\%$  in the  
516 forward direction and  $\pm 2\%$  in the backward direction between the detectors. In

517 addition, the typical deviation inside each site was 4%–7%. These values are smaller  
518 than the statistical error of the observed muons used to determine the density of the  
519 volcanic cone, and thus they were not significant for our observations. It is interesting  
520 to consider if an improvement in the accuracy of the detector position and attitude, and  
521 the DEM, would decrease this systematic error. For example, the  $\pm 4\%$  deviation in the  
522 forward direction would be expected to decrease to  $\pm 2\%$ , because the misfit effect is  
523 less in the backward direction. Further improvements will require simulation of the  
524 expected muon flux that take into account more processes and verification of the  
525 systematic errors associated with the ECC detectors.

526 The obtained density values ( $1.42\text{--}1.53 \times 10^3 \text{ kg m}^{-3}$ ; this study) and  $1.39 \pm 0.07$   
527  $\times 10^3 \text{ kg m}^{-3}$  (Nishiyama et al., 2021) for Izu–Omuroyama scoria cone are broadly  
528 consistent (Table 2). In a previous study, Rosas-Carbajal et al. (2017) identified an  
529 offset between the density obtained by muon and gravity data and the density obtained  
530 from muon data was  $0.5 \times 10^3 \text{ kg m}^{-3}$  less than that obtained from gravity data. In our  
531 validation, this discrepancy does not exist. As Rosas-Carbajal et al (2017) suggested,  
532 the discrepancy might be due to differences in the filtering performance for low-  
533 momentum particles shown in Fig. 9.

534 The higher density obtained at site W cannot be explained by the systematic errors  
535 described above. One possible reason for this is an actual high-density structure in  
536 front of the site. This hypothesis is consistent with the fact that lava flowed out from  
537 the crater lake to the west (Koyano et al., 1996).

538

539 **8 Conclusions**

540 A muographic study of the Izu–Omuroyama scoria cone was undertaken in 11  
541 directions. The ECC detector design was optimized for quick installation in the field.  
542 We mounted the 11 detectors beneath the ground, surrounding the volcanic cone. The  
543 tracks of charged particles that passed through the ECCs were reconstructed using the  
544 automated emulsion track readout system HTS and NETSCAN 2.0 software. After  
545 track selection, including momentum filtering and efficiency estimation, the density  
546 profiles in 2D angular space were derived for each observation site. The methods  
547 described in this paper can be applied to the observation of other volcanoes and target  
548 objects.

549 We compared the observed muon flux to the expected value from a muon flux model in  
550 the free sky region. The muon flux difference between each detector was 4% in the  
551 forward directions and 2% in the backward directions, and the typical deviations in  
552 each site were about 4%–7%. The errors on the detector coordinates and attitude, and  
553 DEM, are the main cause of the discrepancy between the observed and expected muon  
554 flux.

555 In addition, we also compared our results with the overall volcanic cone density  
556 estimated from gravity data, which are broadly consistent, apart from the W site. This  
557 discrepancy for the W site can be explained by the systematic errors discussed in the  
558 previous section and statistical error of the observed muons. It might also reflect a  
559 high-density structure located in the western flank of the volcano. Further 3D density  
560 reconstructions of the Izu–Omuroyama scoria cone are ongoing using the data set  
561 described in this paper.

562

563 **Acknowledgements**

564 The authors thank Hideaki Aoki and his colleagues of Ike-kankou for collaborating on  
565 our study. We also thank Masakazu Ichikawa of the Earthquake Research Institute,  
566 the University of Tokyo, for support during the observation campaign. We are also  
567 grateful for the technical support of the staff and students in F-lab, Nagoya University,  
568 especially with the nuclear emulsion films. This research was supported by JSPS  
569 KAKENHI Grant 19H01988, an Izu Peninsula Geopark Academic Research Grant  
570 (2018), the Joint Research Program of the Institute of Materials and Systems for  
571 Sustainability at Nagoya University (2017–2021), and a JSPS Fellowship (Nagahara;  
572 Grant DC2, 19J13805).

573

574 **References**

- 575 Agafonova, N., Aleksandrov, A., Altinok, O., Anokhina, A., Aoki, S., Ariga, A., Ariga, T.,  
576 Autiero, D., Badertscher, A., Bagulya, A., Ben Dhahbi, A., Bertolin, A., Besnier, M.,  
577 Bozza, C., Brugière, T., Brugnera, R., Brunet, F., Brunetti, G., Buontempo, S., Cazes,  
578 A., Chaussard, L., Chernyavskiy, M., Chiarella, V., Chukanov, A., D'Ambrosio, N., Dal  
579 Corso, F., De Lellis, G., del Amo Sanchez, P., Déclais, Y., De Serio, M., Di Capua, F., Di  
580 Crescenzo, A., Di Ferdinando, D., Di Marco, N., Dmitrievski, S., Dracos, M.,  
581 Duchesneau, D., Dusini, S., Dzhatdoev, T., Ebert, J., Egorov, O., Enikeev, R., Ereditato,  
582 A., Esposito, L. S., Favier, J., Ferber, T., Fini, R. A., Frekers, D., Fukuda, T.,  
583 Garfagnini, A., Giacomelli, G., Giorgini, M., Göllnitz, C., Goldberg, J., Golubkov, D.,  
584 Goncharova, L., Gornushkin, Y., Grella, G., Grianti, F., Guler, A. M., Gustavino, C.,  
585 Hagner, C., Hamada, K., Hara, T., Hierholzer, M., Hollnagel, A., Hoshino, K., Ieva, M.,  
586 Ishida, H., Jakovcic, K., Jollet, C., Juget, F., Kamiscioglu, M., Kazuyama, K., Kim, S.  
587 H., Kimura, M., Kitagawa, N., Klicek, B., Knuesel, J., Kodama, K., Komatsu, M., Kose,  
588 U., Kreslo, I., Kubota, H., Lazzaro, C., Lenkeit, J., Lippi, I., Ljubicic, A., Longhin, A.,  
589 Loverre, P., Lutter, G., Malgin, A., Mandrioli, G., Manai, K., Marteau, J., Matsuo, T.,  
590 Matveev, V., Mauri, N., Medinaceli, E., Meisel, F., Meregaglia, A., Migliozi, P.,  
591 Mikado, S., Miyamoto, S., Monacelli, P., Morishima, K., Moser, U., Muciaccia, M. T.,  
592 Naganawa, N., Naka, T., Nakamura, M., Nakano, T., Naumov, D., Nikitina, V., Niwa,  
593 K., Nonoyama, Y., Ogawa, S., Okateva, N., Olshevskiy, A., Paniccia, M., Paoloni, A.,  
594 Park, B. D., Park, I. G., Pastore, A., Patrizzii, L., Pennacchio, E., Pessard, H., Pretzl, K.,  
595 Pilipenko, V., Pistillo, C., Polukhina, N., Pozzato, M., Pupilli, F., Rescigno, R.,  
596 Roganova, T., Rokujo, H., Romano, G., Rosa, G., Rostovtseva, I., Rubbia, A., Russo, A.,  
597 Ryasny, V., Ryazhskaya, O., Sato, O., Sato, Y., Schembri, A., Schmidt-Parzefall, W.,

598 Schroeder, H., Scotto Lavina, L., Sheshukov, A., Shibuya, H., Shoziyoev, G., Simone, S.,  
599 Sioli, M., Sirignano, C., Sirri, G., Song, J. S., Spinetti, M., Stanco, L., Starkov, N.,  
600 Stipcevic, M., Strauss, T., Strolin, P., Takahashi, S., Tenti, M., Terranova, F., Tezuka,  
601 I., Tioukov, V., Tolun, P., Trabelsi, A., Tran, T., Tufanli, S., Vilain, P., Vladimirov, M.,  
602 Votano, L., Vuilleumier, J. L., Wilquet, G., Wonsak, B., Yakushev, V., Yoon, C. S.,  
603 Yoshioka, T., Yoshida, J., Zaitsev, Y., Zemskova, S., Zghiche, A., and Zimmermann, R.:  
604 Momentum measurement by the multiple Coulomb scattering method in the OPERA  
605 lead-emulsion target, *New J. Phys.*, 14, 013026, [https://doi.org/10.1088/1367-](https://doi.org/10.1088/1367-2630/14/1/013026)  
606 [2630/14/1/013026](https://doi.org/10.1088/1367-2630/14/1/013026), 2012.  
607  
608 Aramaki, S., and Hamuro, K.: Geology of the Higasi–Izu monogenetic volcano group,  
609 *Bull. Earthq. Res. Inst. Univ. Tokyo*, 52, 235–278, [https://repository.dl.itc.u-](https://repository.dl.itc.u-tokyo.ac.jp/record/33207/files/ji0522010.pdf)  
610 [tokyo.ac.jp/record/33207/files/ji0522010.pdf](https://repository.dl.itc.u-tokyo.ac.jp/record/33207/files/ji0522010.pdf), 1977. (in Japanese)  
611  
612 Bozza, C., D’Ambrosio, N., De Lellis, G., De Serio, M., Di Capua, F., Di Crescenzo, A.,  
613 Di Ferdinando, D., Di Marco, N., Esposito, L. S., Rosa Anna Fini, R. A., Giacomelli, G.,  
614 Grella, G., Ieva, M., Kose, U., Longhin, A., Mauri, N., Medinaceli, E., Monacelli, P.,  
615 Muciaccia, M. T., Pastore, A., Patrizii, L., Pozzato, M., Pupilli, F., Rescigno, R.,  
616 Romano, G., Rosa, G., Ruggieri, A., Russo, A., Simone, S., Sirignano, C., Sirri, G.,  
617 Stellacci, S. M., Tenti, M., Tioukov, V., Togo, V., and Valieri, C.: An integrated system  
618 for large scale scanning of nuclear emulsions, *Nucl. Instrum. Methods Phys. Res. A*,  
619 703, 1, 204–212, <https://doi.org/10.1016/j.nima.2012.11.099>, 2012.  
620  
621 Bush, A. L.: Construction Materials: Lightweight Aggregates, in “Encyclopedia of

622 Materials: Science and Technology”, Elsevier, pp 1550–1558, <https://doi.org/10.1016/B0->  
623 [08-043152-6/00277-1](https://doi.org/10.1016/B0-08-043152-6/00277-1), 2001.

624

625 Geshi, N., and Neri, M.: Dynamic feeder dyke systems in basaltic volcanoes: the  
626 exceptional example of the 1809 Etna eruption (Italy), *Front. Earth Sci.*, 2, 13,  
627 <https://doi.org/10.3389/feart.2014.00013>, 2014.

628

629 Groom, D. E., Mokhov, N. V., and Striganov, S. I.: Muon stopping power and range  
630 tables 10 MeV–100 TeV, *At. Data Nucl. Data Tables* , 78, 183–356,  
631 <https://doi.org/10.1006/adnd.2001.0861>, 2001.

632

633 Hamada, K., Fukuda, T., Ishiguro, K., Kitagawa, N., Kodama, K., Komatsu, M.,  
634 Morishima, K., Nakano, T., Nakatsuka, Y., Nonoyama, Y., Sato, O., and Yoshida, J.:  
635 Comprehensive track reconstruction tool “NETSCAN 2.0” for the analysis of the  
636 OPERA Emulsion Cloud Chamber, *J. Instrum.*, 7, P07001, <https://doi.org/10.1088/1748->  
637 [0221/7/07/P07001](https://doi.org/10.1088/1748-0221/7/07/P07001), 2012.

638

639 Hamuro, K.: Petrology of the Higashi–Izu monogenetic volcano group, *Bull. Earthq.*  
640 *Res. Inst. Univ. Tokyo*, 60, 335–400, [https://repository.dl.itc.u-](https://repository.dl.itc.u-tokyo.ac.jp/record/32886/files/ji0603001.pdf)  
641 [tokyo.ac.jp/record/32886/files/ji0603001.pdf](https://repository.dl.itc.u-tokyo.ac.jp/record/32886/files/ji0603001.pdf), 1985.

642

643 Hiramoto, A., Suzuki, Y., Ali, A., Aoki, S., Berns, L., Fukuda, T., Hanaoka, Y., Hayato,  
644 Y., Ichikawa, A. K., Kawahara, H., Kikawa, T., Koga, T., Komatani, R., Komatsu, M.,  
645 Kosakai, Y., Matsuo, T., Mikado, S., Minamino, A., Mizuno, K., Morimoto, Y.,

646 Morishima, K., Naganawa, N., Naiki, M., Nakamura, M., Nakamura, Y., Nakano, N.,  
647 Nakano, T., Nakaya, T., Nishio, A., Odagawa, T., Ogawa, S., Oshima, H., Rokujo, H.,  
648 Sanjana, I., Sato, O., Shibuya, H., Sugimura, K., Suzui, L., Takagi, H., Takao, T.,  
649 Tanihara, Y., Yasutome, K., and Yokoyama, M. (NINJA Collaboration): First  
650 measurement of  $\bar{\nu}_\mu$  and  $\nu_\mu$  charged-current inclusive interactions on water using a  
651 nuclear emulsion detector, *Phys. Rev. D*, 102, 072006,  
652 <https://doi.org/10.1103/PhysRevD.102.072006>, 2020.  
653  
654 Honda, M., Kajita, T., Kasahara, K., and Midorikawa, S.: New calculation of the  
655 atmospheric neutrino flux in a three-dimensional scheme, *Phys. Rev. D*, 70, 043008,  
656 <https://doi.org/10.1103/PhysRevD.70.043008>, 2004.  
657  
658 Jourde, K., Gibert, D., and Marteau, J.: Improvement of density models of geological  
659 structures by fusion of gravity data and cosmic muon radiographies, *Geosci. Instrum.*  
660 *Methods Data Syst.*, 4, 177–188, <https://doi.org/10.5194/gi-4-177-2015>, 2015.  
661  
662 Jourde, K., Gibert, D., Marteau, J., d'Ars, J.B., and Komorowski, J.C.: Muon dynamic  
663 radiography of density changes induced by hydrothermal activity at the La Soufrière of  
664 Guadeloupe volcano, *Sci. Rep.*, 6, 33406, <https://doi.org/10.1038/srep33406>, 2016.  
665  
666 Kereszturi, G., and Németh, K.: *Monogenetic Basaltic Volcanoes: Genetic*  
667 *Classification, Growth, Geomorphology and Degradation, Updates in Volcanology—*  
668 *New Advances in Understanding Volcanic Systems*, Karoly Nemeth, IntechOpen., DOI:  
669 10.5772/51387, 2012.

670

671 Kodama, K., Hoshino, K., Komatsu, M., Miyanishi, M., Nakamura, M., Nakamura, T.,  
672 Nakano, T., Narita, K., Niwa, K., Nonaka, N., Sato, O., Toshito, T., and Uetake, T.:  
673 Study of electron identification in a few GeV region by an emulsion cloud chamber,  
674 Rev. Sci. Instrum., 74, 53, <https://doi.org/10.1063/1.1529300>, 2003.

675

676 Koyama, M.: Photographs of the Izu-peninsula by UAV, Iwanami Science Library 268,  
677 Iwanami Shoten, Publishers, Tokyo, 159 pp, ISBN 9784000296687, 2017. (in Japanese)

678

679 Koyano, Y., Hayakawa, Y., and Machida, H.: The eruption of Omuroyama in the  
680 Higashi Izu monogenetic volcano field, J Geog. (Chigaku Zasshi), 105, 4, 475–484,  
681 <https://doi.org/10.5026/jgeography.105.4.475>, 1996. (in Japanese)

682

683 Kreslo, I., Cozzi, M., Ereditato, A., Hess, M., Knuesel, J., Laktineh, I., Messina, M.,  
684 Moser, U., Pistillo, C., and Pretzl, K.: High-speed analysis of nuclear emulsion films  
685 with the use of dry objective lenses, J. Instrum., 3, P04006,  
686 <https://dx.doi.org/10.1088/1748-0221/3/04/P04006>, 2008.

687

688 Morishima, K., and Nakano, T.: Development of a new automatic nuclear emulsion  
689 scanning system, S-UTS, with continuous 3D tomographic image read-out, J. Instrum.,  
690 5, P04011, <http://dx.doi.org/10.1088/1748-0221/5/04/P04011>, 2010.

691

692 Morishima, K., Kuno, M., Nishio, A., Kitagawa, N., Manabe, Y., Moto, M., Takasaki, F.,  
693 Fujii, H., Satoh, K., Kodama, H., Hayashi, K., Odaka, S., Procureur, S., Attie, D.,

694 Bouteille, S., Calvet, D., Filosa, C., Magnier, P., Mandjavidze, I., Riallot, M., Marini, B.,  
695 Gable, P., Date, Y., Sugiura, M., Elshayeb, Y., Elnady, T., Ezzy, M., Guerriero, E.,  
696 Steiger, V., Serikoff, N., Mouret, J., Charles, B., Helal, H., and Tayoubi, M.: Discovery  
697 of a big void in Khufu's Pyramid by observation of cosmic-ray muons, *Nature*, 552, 387,  
698 <https://doi.org/10.1038/nature24647>, 2017.

699

700 Nagahara, S., and Miyamoto, S.: Feasibility of three-dimensional density tomography  
701 using dozens of muon radiographies and filtered back projection for volcanoes, *Geosci.*  
702 *Instrum. Methods Data Syst.*, 7, 307–316, <https://doi.org/10.5194/gi-7-307-2018>, 2018.

703

704 Nakamura, T., Ariga, A., Ban, T., Fukuda, T., Fukuda, T., Fujioka, T., Furukawa, T.,  
705 Hamada, K., Hayashi, H., Hiramatsu, S., Hoshino, K., Kawada, J., Koike, N., Komatsu,  
706 M., Matsuoka, H., Miyamoto, S., Miyanishi, K., Miyanishi, M., Morishima, K., Nada,  
707 H., Naganawa, N., Nakano, T., Narita, K., Natsume, M., Niwa, K., Nonaka, N., Park,  
708 B. D., Sato, O., Takahashi, S., Toshito, T., Uetake, T., Nakamura, M., Kuwabara, K.,  
709 Nishiyama, S., Nonoyama, Y., and Kodama, K.: The OPERA film: New nuclear  
710 emulsion for large-scale, high-precision experiments, *Nucl. Instrum. Methods Phys.*  
711 *Res. A*, 556, 1, 80–86, <https://doi.org/10.1016/j.nima.2005.08.109>, 2005.

712

713 Nishio, A., Morishima, K., Kuwabara, K., Yoshida, T., Funakubo, T., Kitagawa, N.,  
714 Kuno, M., Manabe, Y., and Nakamura, M.: Nuclear emulsion with excellent long-term  
715 stability developed for cosmic-ray imaging, *Nuclear Instruments and Methods in*  
716 *Physics Research A*, 966, 163850, <https://doi.org/10.1016/j.nima.2020.163850>, 2020.

717

718 Nishiyama, R., Miyamoto, S., and Naganawa, N.: Experimental study of source of  
719 background noise in muon radiography using emulsion film detectors, *Geosci. Instrum.*  
720 *Methods Data Syst.*, 3, 29–39, <https://doi.org/10.5194/gi-3-29-2014>, 2014.

721

722 Nishiyama, R., Miyamoto, S., Okubo, S., Oshima, H., and Maekawa, T.: 3D density  
723 modeling with gravity and muon-radiographic observations in Showa–Shinzan lava  
724 dome, Usu, Japan, *Pure Appl. Geophys.*, 174, 1061–1070,  
725 <https://doi.org/10.1007/s00024-016-1430-9>, 2017.

726

727 Nishiyama, R., Miyamoto, S., and Nagahara, S.: Estimation of the bulk density of the  
728 Omuro scoria cone (eastern Izu, Japan) from gravity survey, *Bull. Earthq. Res. Inst.*  
729 *Univ. Tokyo*, 95, 1–7, [https://repository.dl.itc.u-](https://repository.dl.itc.u-tokyo.ac.jp/record/2000093/files/IHO951401.pdf)  
730 [tokyo.ac.jp/record/2000093/files/IHO951401.pdf](https://repository.dl.itc.u-tokyo.ac.jp/record/2000093/files/IHO951401.pdf), 2020.

731

732 Oláh, L., Tanaka, H. K. M., Ohminato, T., and Varga, D.: High-definition and low-noise  
733 muography of the Sakurajima volcano with gaseous tracking detectors, *Sci. Rep.*, 8,  
734 3207, <https://doi.org/10.1038/s41598-018-21423-9>, 2018.

735

736 Rosas-Carbajal, M., Jourde, K., Marteau, J., Deroussi, S., Komorowski, J.-C., and  
737 Gibert, D.: Three-dimensional density structure of La Soufrière de Guadeloupe lava  
738 dome from simultaneous muon radiographies and gravity data, *Geophys. Res. Lett.*, 44,  
739 6743–6751, <https://doi.org/10.1002/2017GL074285>, 2017.

740

741 Saito, T., Takahashi, S., and Wada, H.:  $^{14}\text{C}$  ages of Omuroyama Volcano, Izu Peninsula,

742 Bull. Volcanol. Soc. Jpn. , 48, 215–219, [https://doi.org/10.18940/kazan.48.2\\_215](https://doi.org/10.18940/kazan.48.2_215), 2003.  
743 (in Japanese)  
744  
745 Saracino, G., Amato, L., Ambrosino, F., Antonucci, G., Bonechi, L., Cimmino, L.,  
746 Consiglio, L., D'Alessandro, R., De Luzio, E., Minin, G., Noli, P., Scognamiglio, L.,  
747 Strolin, P., and Varriale, A.: Imaging of underground cavities with cosmic-ray muons  
748 from observations at Mt. Echia (Naples), Sci. Rep., 7, 1181,  
749 <https://doi.org/10.1038/s41598-017-01277-3>, 2017.  
750  
751 Taha, A. A., and Mohamed, A. A.: Chemical, physical and geotechnical properties  
752 comparison between scoria and pumice deposits in Dhamar–Rada Volcanic Field, SW  
753 Yemen, Aust. J. Basic & Appl. Sci., 7, 11, 116–124,  
754 <http://www.ajbasweb.com/old/ajbas/2013/September/116-124.pdf>, 2013.  
755  
756 Takahashi, S., Aoki, S., Kamada, K., Mizutani, S., Nakagawa, R., Ozaki, K., and  
757 Rokujo, H.: GRAINE project: The first balloon-borne, emulsion gamma-ray telescope  
758 experiment, Prog. Theor. Exp. Phys., 4, <https://doi.org/10.1093/ptep/ptv046>, 2015.  
759  
760 Tanahashi, M., et al. (Particle Data Group), Phys. Rev. D 98, 030001,  
761 <https://doi.org/10.1103/PhysRevD.98.030001>, 2018.  
762  
763 Tanaka, H. K. M., Nakano, T., Takahashi, S., Yoshida, J., Takeo, M., Oikawa, J.,  
764 Ohminato, T., Aoki, Y., Koyama, E., Tsuji, H., and Niwa, K.: High resolution imaging  
765 in the inhomogeneous crust with cosmic-ray muon radiography: The density structure

766 below the volcanic crater floor of Mt. Asama, Japan, *Earth Planet. Sci. Lett.*, 263, 1–2,  
767 104–113, <https://doi.org/10.1016/j.epsl.2007.09.001>, 2007.

768

769 Tanaka, H. K. M., Uchida, T., Tanaka, M., Shinohara, H., and Hideaki, T.: Cosmic-ray  
770 muon imaging of magma in a conduit: Degassing process of Satsuma–Iwojima Volcano,  
771 Japan, *Geophys. Res. Lett.*, 36, L01304, <https://doi.org/10.1029/2008GL036451>, 2009.

772

773 Tanaka, H. K. M., Taira, H., Uchida, T., Tanaka, M., Takeo, M., Ohiminato, T., and  
774 Tsuji, H.: Three-dimensional computational axial tomography scan of a volcano with  
775 cosmic ray muon radiography, *J. Geophys. Res. Solid Earth*, 115, B12332,  
776 <https://doi.org/10.1029/2010JB007677>, 2010.

777

778 Tanaka, H. K. M., Kusagaya, T., and Shinohara, H.: Radiographic visualization of  
779 magma dynamics in an erupting volcano, *Nat. Commun.*, 5, 3381,  
780 <https://doi.org/10.1038/ncomms4381>, 2014.

781

782 Tioukov, V., Alexandrov, A., Bozza, C., Consiglio, L., D'Ambrosio, N., De Lellis, G., De  
783 Sio, C., Giudicepietro, F., Macedonio, G., Miyamoto, S., Nishiyama, R., Orazi, M.,  
784 Peluso, R., Sheshukov, A., Sirignano, C., Stellacci, S. M., Strolin, P., and Tanaka, H. K.  
785 M.: First muography of Stromboli volcano, *Sci. Rep.*, 9, 6695,  
786 <https://doi.org/10.1038/s41598-019-43131-8>, 2019.

787

788 Watanabe, A., Takenaka, H., Fujii, Y., and Fujiwara, H.: Seismometer azimuth  
789 measurement at K-NET station (2): Oita Prefecture, *Zisin*, 53, 185–192,

790 [https://doi.org/10.4294/zisin1948.53.2\\_185](https://doi.org/10.4294/zisin1948.53.2_185), 2000. (in Japanese)

791

792 Yamamoto, H.: The mode of lava outflow from cinder cones in the Ojika–Jima

793 monogenetic volcano group, Bull. Volcanol. Soc. Jpn., 48, 1,

794 [https://doi.org/10.18940/kazan.48.1\\_11](https://doi.org/10.18940/kazan.48.1_11), 2003. (in Japanese)

795

796 Yoshimoto, M., Nakano, T., Komatani, R., and Kawahara, H.: Hyper-track selector

797 nuclear emulsion readout system aimed at scanning an area of one thousand square

798 meters, Prog. Theor. Exp. Phys., 2017, 10, <https://doi.org/10.1093/ptep/ptx131>, 2017.

799

800 **Appendix A**

801 We here consider how the position dependency of the detected tracks affects the density  
802 results.

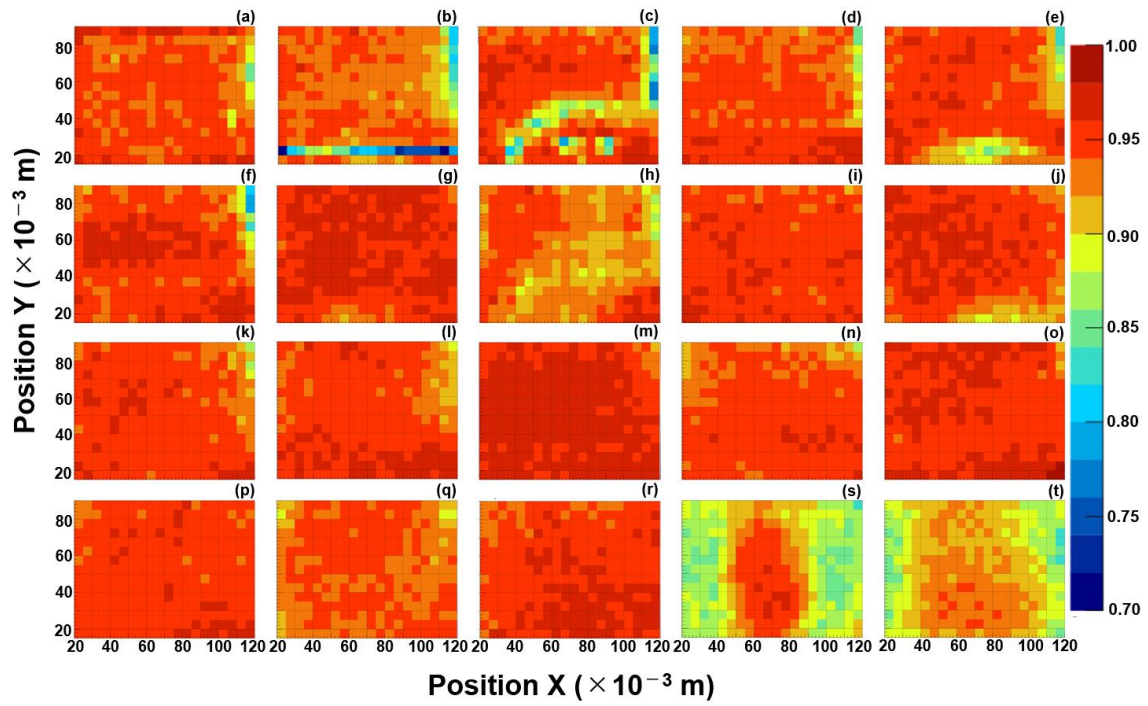
803 The fill factor of the base tracks (i.e., track detection efficiency in a film) also depends  
804 on the position of the scanned film. The typical causes of the decrease of the fill factor  
805 are heterogeneous thickness of the emulsion layers, some dusts or scratches on the  
806 emulsion surface, and the poorly tuned parameters for the scanning.

807 Fig. 15 shows the position distribution of the fill factor of all films of an ECC. For  
808 example, at upper right the films tend to have the low fill factor (e.g., a-f, h, k, l, q). This  
809 part has the larger thickness of emulsion layer because the drops of glycerin solution  
810 were left in the upper right corner when drying after soaking due to the structure of  
811 developing racks. Fig. 15(s) and (t) have larger area of low fill factor in the right and left.  
812 The reason might be the poorly tuned parameters for the scanning.

813 Compared to the size of the scoria cone, the ECC is a very small “element”, thus the  
814 local position dependence of the fill factor can be approximately treated as an average  
815 fill factor  $\varepsilon_j(\theta_x, \theta_y)$ . The decrease of the fill factor is reflected in the  $\varepsilon_j(\theta_x, \theta_y)$  in Eq. (4).  
816 Finally,  $\varepsilon_j(\theta_x, \theta_y)$ , which encompasses the effects of the local decrease of the fill factor, is  
817 effectively used to derive the angle-dependent muon detection efficiency.

818 We should also consider the position dependency of noise. Local high density of random  
819 silver grains caused by any chemical conditions, or fake images produced by scratches  
820 on the films tend to create a group of fake tracks concentrated in one place. In addition,  
821 such fake tracks tend to have small slopes by scanning with automated emulsion readout  
822 system. If such noise is continuous at the same location on the film, they might make  
823 many parallel tracks at a certain slope and give a systematic error in the result. However,  
824 such possibility has been eliminated by the track selection algorithm described in the  
825 section 4.2. Because such concentrated tracks in position and angular space make  
826 numerous branches in track connection (see Fig. 6) and tracks with such branches were  
827 removed in the selection procedure. Fig. 16 shows the number of selected tracks with  
828 small slope per mm<sup>2</sup> in each observation site. The histogram roughly fits the Poisson  
829 distribution and there is no remarkable excess. The difference of the peak in the  
830 histograms depends on the difference of exposure time (SE, W, NNE), existence of  
831 topography in the backward direction (NE), pitch angle of the detector attitude (e.g., SW  
832 has larger pitch angle, thus less tracks of the small slopes from the backward direction),  
833 and the difference of muon detection efficiency.

834

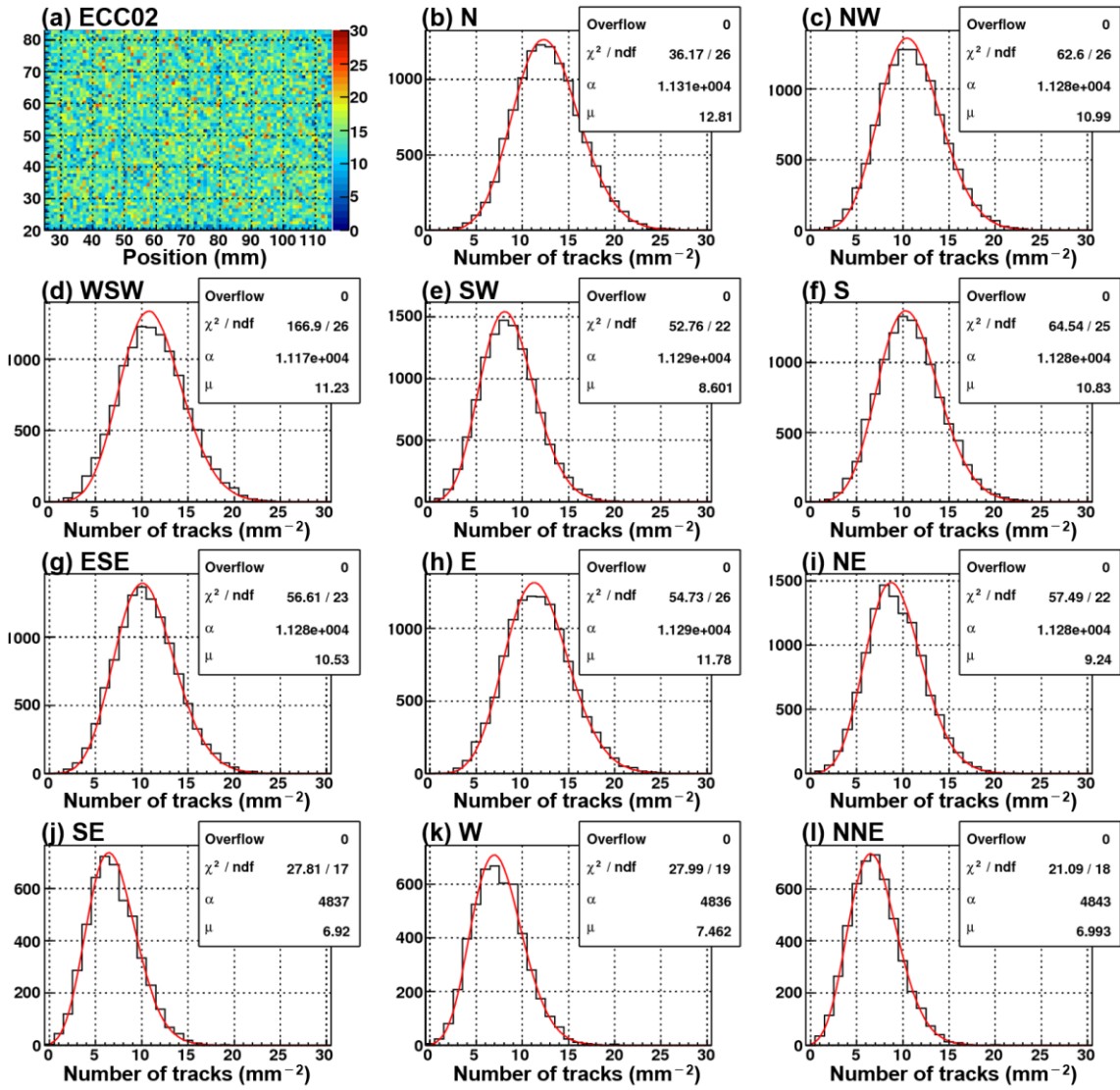


835

836

837 Figure 15. The position distribution of the fill factor in each film of ECC02. (a)–(t)  
838 represent PL01–PL20, respectively.

839



841

842

843 Figure 16. (a) The position distribution of the number of the selected tracks per  $\text{mm}^2$  in  
 844 the ECC02. (b)–(l) The number of the selected tracks per  $\text{mm}^2$  (the black line) with the  
 845 fitting result of Poisson distribution ( $= \alpha \mu^x e^{-\mu} / x!$ , the red line) in each observation  
 846 site, respectively. The tracks selected for this figure came from in the backward  
 847 direction and have small slopes ( $|\tan \theta_x| < 0.5$  and  $|\tan \theta_y| < 0.5$ ).

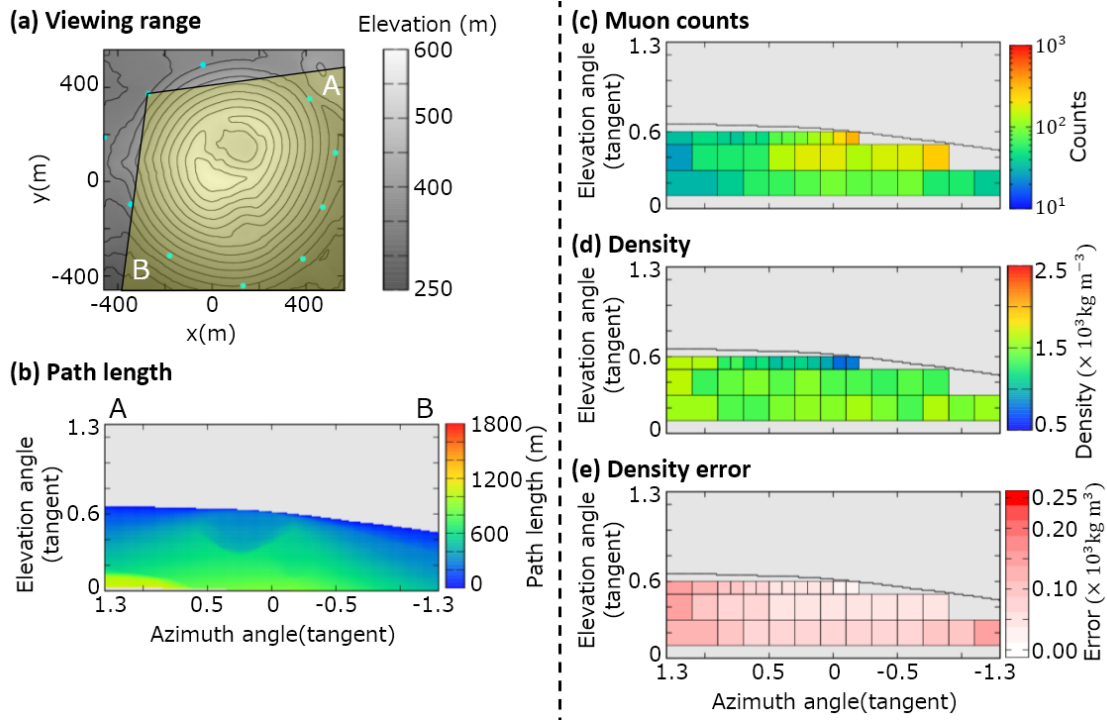
848

849

850 **Appendix B**

851 The density results for each observation site are shown in Figs 17–26.

852



853

854

855 Figure 17. Observation site NW. (a) Map, topography, and viewing range; (b) path

856 length of the volcanic cone; (c) muon counts  $N_i^{obs}$ ; (d) density  $\rho_i$ . The maximum value of

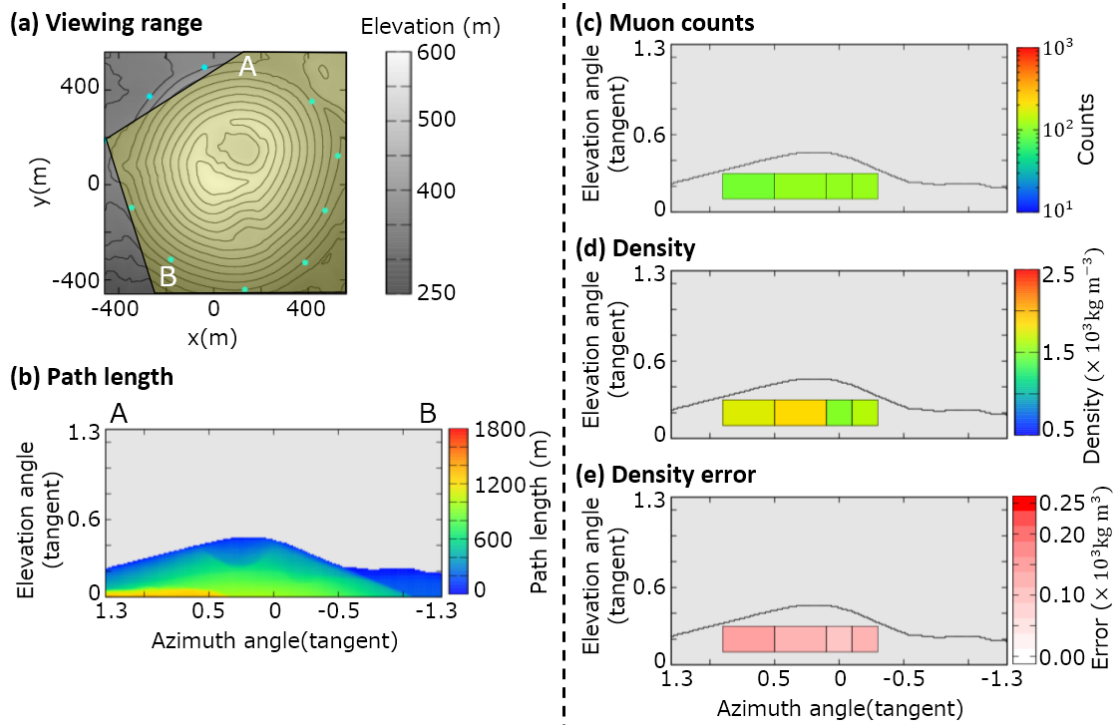
857 the color bar indicates a density of  $>2.5 \times 10^3 \text{ kg m}^{-3}$  and the minimum value is  $<0.5$

858  $\times 10^3 \text{ kg m}^{-3}$ . (e) Density error  $\Delta\rho = (\rho_i^{up} - \rho_i^{low})/2$ . The maximum value of the color

859 bar indicates a density error of  $>0.25 \times 10^3 \text{ kg m}^{-3}$ .

860

861



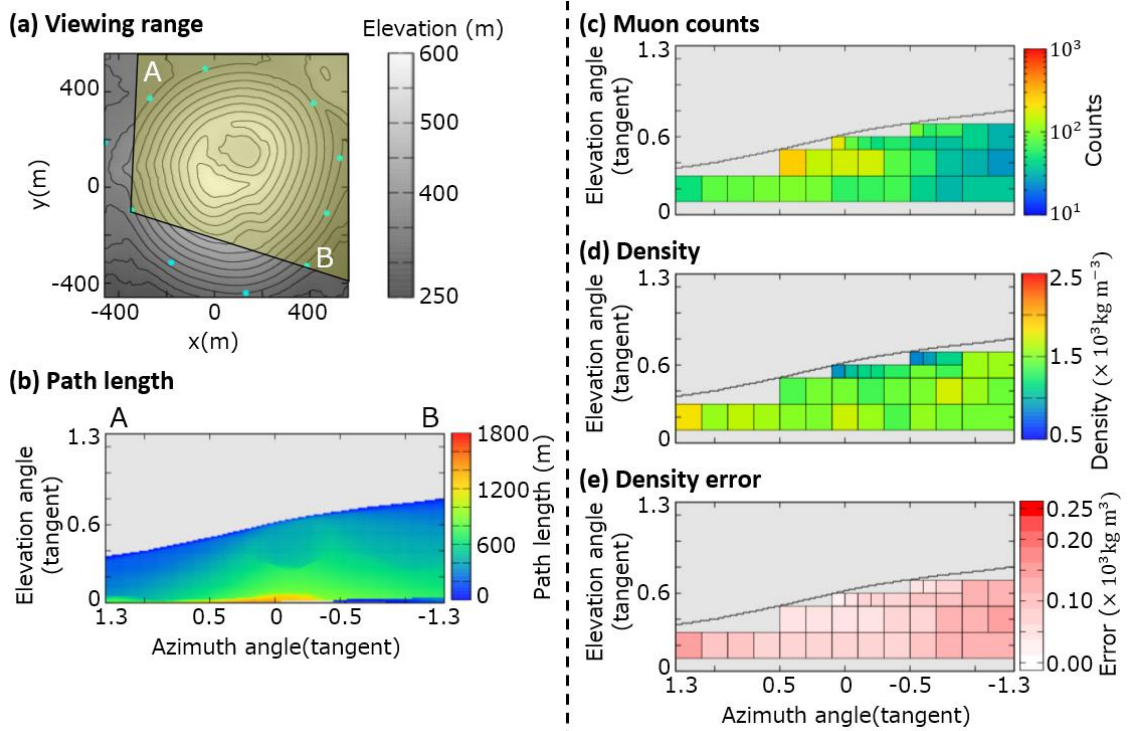
862

863

864 Figure 18. Observation site W. (a) Map, topography, and viewing range; (b) path length  
 865 of the volcanic cone; (c) muon counts  $N_i^{obs}$ ; (d) density  $\rho_i$ . The maximum value of the  
 866 color bar indicates a density of  $>2.5 \times 10^3 \text{ kg m}^{-3}$  and the minimum value is  $<0.5 \times 10^3$   
 867  $\text{kg m}^{-3}$ . (e) Density error  $\Delta\rho = (\rho_i^{up} - \rho_i^{low})/2$ . The maximum value of the color bar  
 868 indicates a density error of  $>0.25 \times 10^3 \text{ kg m}^{-3}$ .

869

870



871

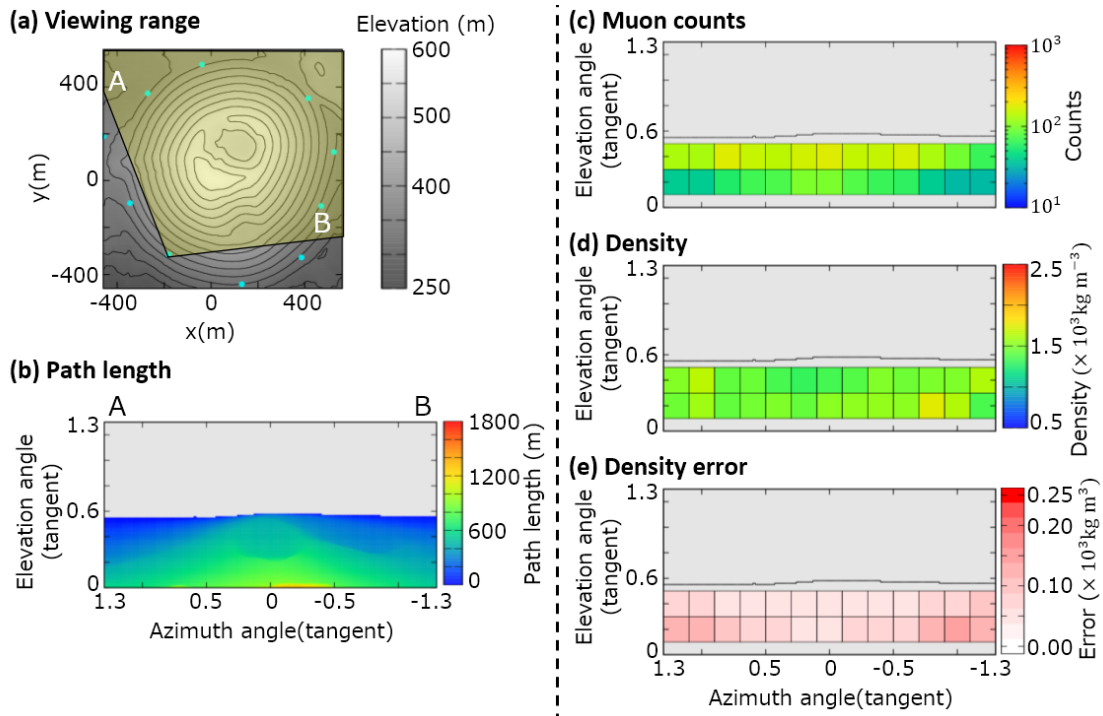
872

873 Figure 19. Observation site WSW. (a) Map, topography, and viewing range; (b) path  
 874 length of the volcanic cone; (c) muon counts  $N_i^{obs}$ ; (d) density  $\rho_i$ . The maximum value of  
 875 the color bar indicates a density of  $>2.5 \times 10^3 \text{ kg m}^{-3}$  and the minimum value is  $<0.5$   
 876  $\times 10^3 \text{ kg m}^{-3}$ . (e) Density error  $\Delta\rho = (\rho_i^{up} - \rho_i^{low})/2$ . The maximum value of the color  
 877 bar indicates a density error of  $>0.25 \times 10^3 \text{ kg m}^{-3}$ .

878

879

880



881

882

883 Figure 20. Observation site SW. (a) Map, topography, and viewing range; (b) path

884 length of the volcanic cone; (c) muon counts  $N_i^{obs}$ ; (d) density  $\rho_i$ . The maximum value of

885 the color bar indicates a density of  $>2.5 \times 10^3 \text{ kg m}^{-3}$  and the minimum value is  $<0.5$

886  $\times 10^3 \text{ kg m}^{-3}$ . (e) Density error  $\Delta\rho = (\rho_i^{up} - \rho_i^{low})/2$ . The maximum value of the color

887 bar indicates a density error of  $>0.25 \times 10^3 \text{ kg m}^{-3}$ .

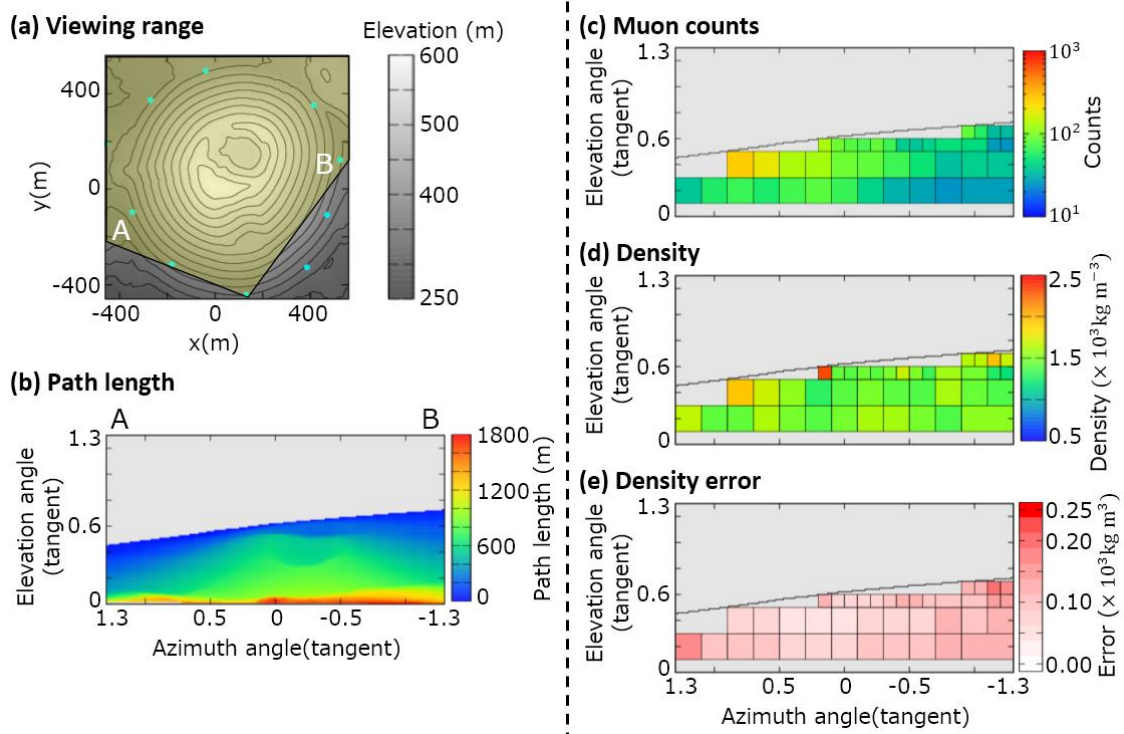
888

889

890

891

892



893

894

895 Figure 21. Observation site S. (a) Map, topography, and viewing range; (b) path length

896 of the volcanic cone; (c) muon counts  $N_i^{obs}$ ; (d) density  $\rho_i$ . The maximum value of the

897 color bar indicates a density of  $>2.5 \times 10^3 \text{ kg m}^{-3}$  and the minimum value is  $<0.5 \times 10^3$

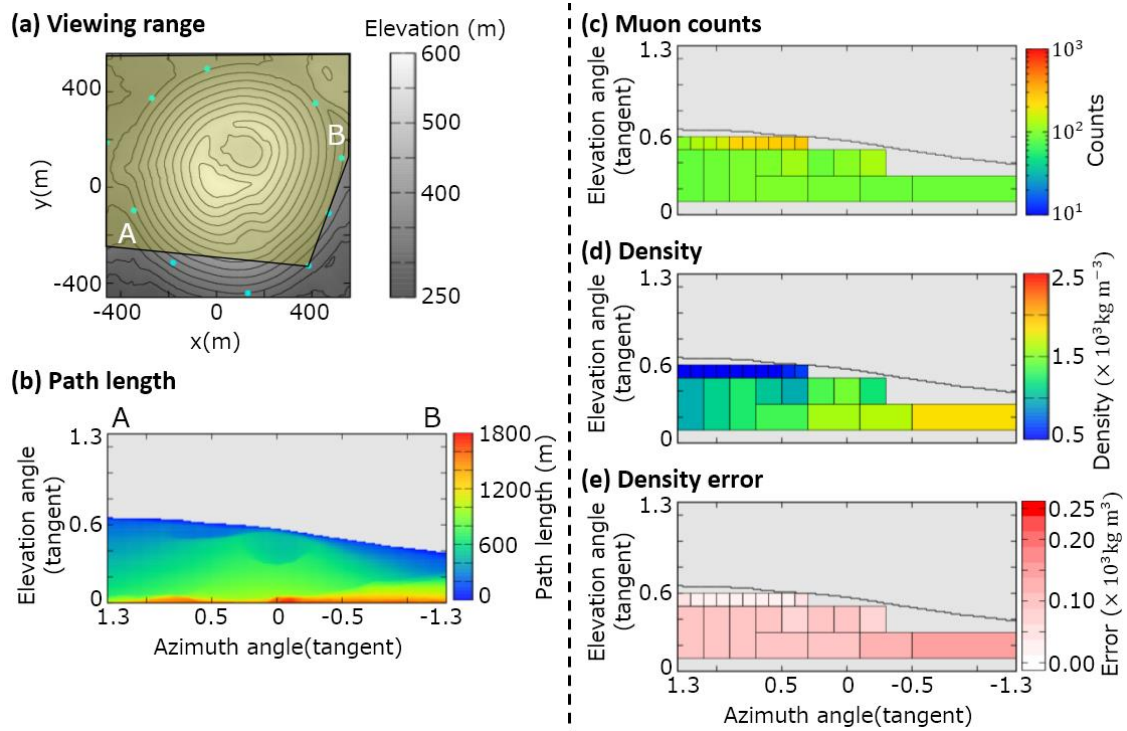
898  $\text{kg m}^{-3}$ . (e) Density error  $\Delta\rho = (\rho_i^{up} - \rho_i^{low})/2$ . The maximum value of the color bar

899 indicates a density error of  $>0.25 \times 10^3 \text{ kg m}^{-3}$ .

900

901

902



903

904

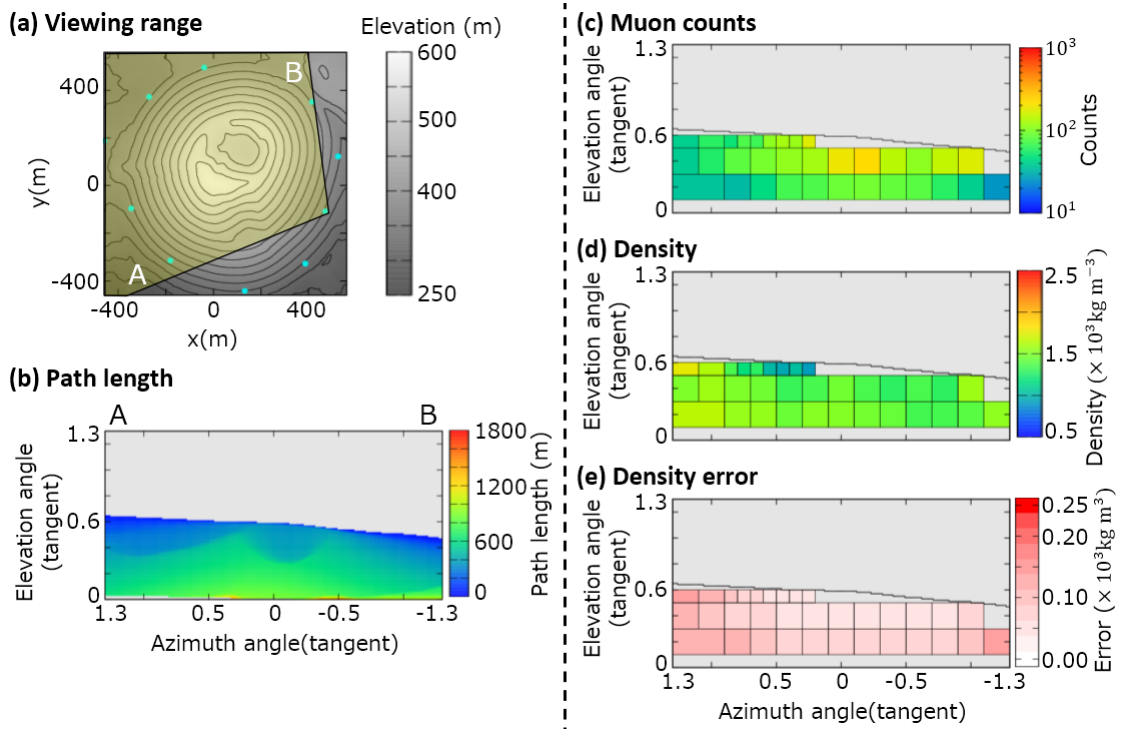
905 Figure 22. Observation site SE. (a) Map, topography, and viewing range; (b) path  
 906 length of the volcanic cone; (c) muon counts  $N_i^{obs}$ ; (d) density  $\rho_i$ . The maximum value of  
 907 the color bar indicates a density of  $>2.5 \times 10^3 \text{ kg m}^{-3}$  and the minimum value is  $<0.5$   
 908  $\times 10^3 \text{ kg m}^{-3}$ . (e) Density error  $\Delta\rho = (\rho_i^{up} - \rho_i^{low})/2$ . The maximum value of the color  
 909 bar indicates a density error of  $>0.25 \times 10^3 \text{ kg m}^{-3}$ .

910

911

912

913



914

915

916 Figure 23. Observation site ESE. (a) Map, topography, and viewing range; (b) path

917 length of the volcanic cone; (c) muon counts  $N_i^{obs}$ ; (d) density  $\rho_i$ . The maximum value of

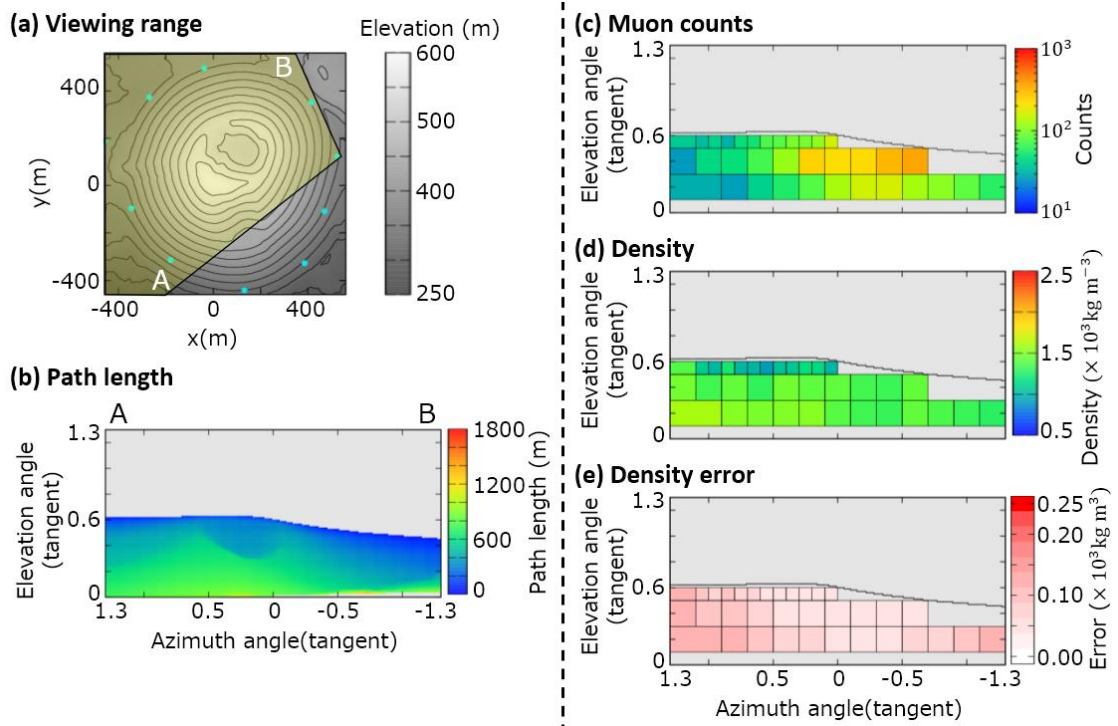
918 the color bar indicates a density of  $>2.5 \times 10^3 \text{ kg m}^{-3}$  and the minimum value is  $<0.5$

919  $\times 10^3 \text{ kg m}^{-3}$ . (e) Density error  $\Delta\rho = (\rho_i^{up} - \rho_i^{low})/2$ . The maximum value of the color

920 bar indicates a density error of  $>0.25 \times 10^3 \text{ kg m}^{-3}$ .

921

922



923

924

925 Figure 24. Observation site E. (a) Map, topography, and viewing range; (b) path length

926 of the volcanic cone; (c) muon counts  $N_i^{obs}$ ; (d) density  $\rho_i$ . The maximum value of the

927 color bar indicates a density of  $>2.5 \times 10^3 \text{ kg m}^{-3}$  and the minimum value is  $<0.5 \times 10^3$

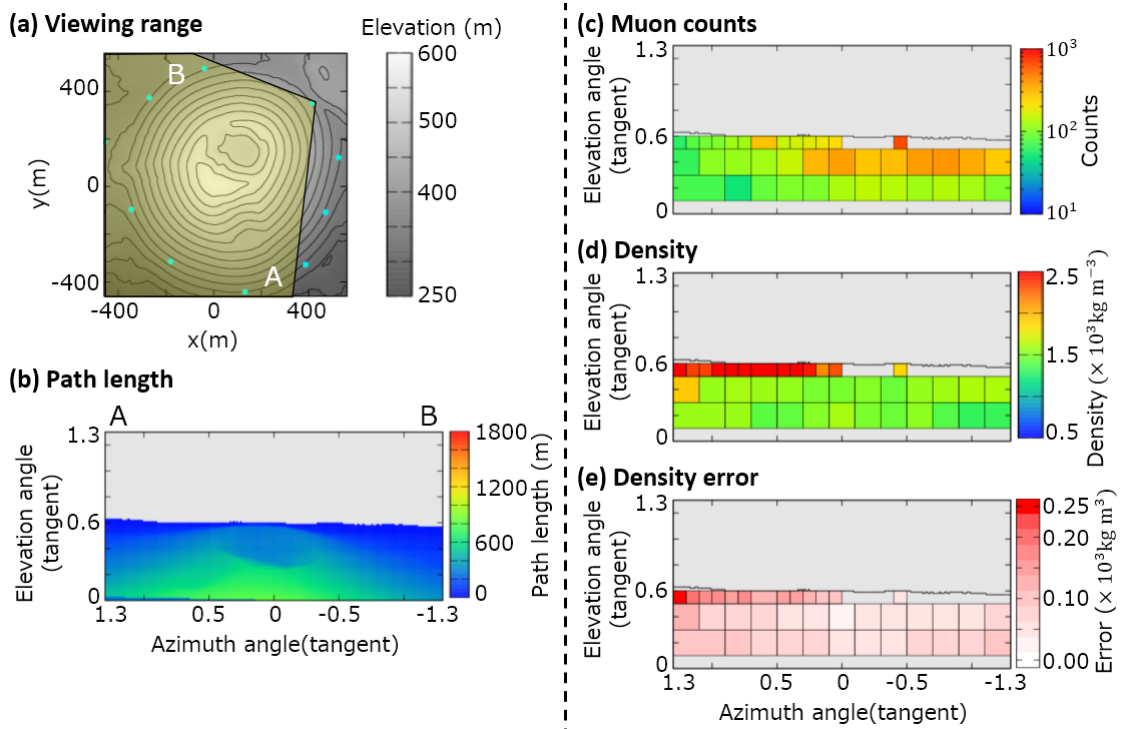
928  $\text{kg m}^{-3}$ . (e) Density error  $\Delta\rho = (\rho_i^{up} - \rho_i^{low})/2$ . The maximum value of the color bar

929 indicates a density error of  $>0.25 \times 10^3 \text{ kg m}^{-3}$ .

930

931

932



934

935

936 Figure 25. Observation site NE. (a) Map, topography, and viewing range; (b) path

937 length of the volcanic cone; (c) muon counts  $N_i^{obs}$ ; (d) density  $\rho_i$ . The maximum value of

938 the color bar indicates a density of  $>2.5 \times 10^3 \text{ kg m}^{-3}$  and the minimum value is  $<0.5$

939  $\times 10^3 \text{ kg m}^{-3}$ . (e) Density error  $\Delta\rho = (\rho_i^{up} - \rho_i^{low})/2$ . The maximum value of the color

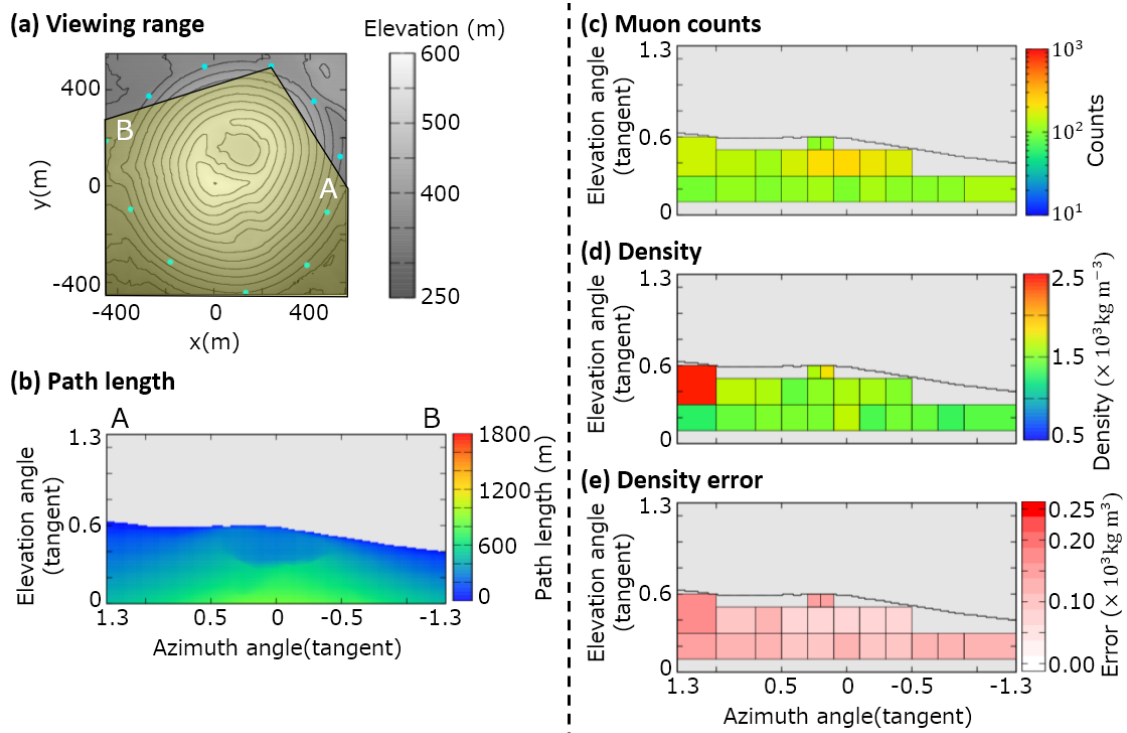
940 bar indicates a density error of  $>0.25 \times 10^3 \text{ kg m}^{-3}$ .

941

942

943

944



945

946

947 Figure 26. Observation site NNE. (a) Map, topography, and viewing range; (b) path

948 length of the volcanic cone; (c) muon counts  $N_i^{obs}$ ; (d) density  $\rho_i$ . The maximum value of

949 the color bar indicates a density of  $>2.5 \times 10^3 \text{ kg m}^{-3}$  and the minimum value is  $<0.5$

950  $\times 10^3 \text{ kg m}^{-3}$ . (e) Density error  $\Delta\rho = (\rho_i^{up} - \rho_i^{low})/2$ . The maximum value of the color

951 bar indicates a density error of  $>0.25 \times 10^3 \text{ kg m}^{-3}$ .

952

953